Microstructure turbulence and diffusivity parameterization in the tropical and subtropical Atlantic, Pacific and Indian Oceans during the Malaspina 2010 expedition

B. Fernández-Castro [a,*], B. Mouriño-Carballido [a], V.M. Benítez-Barrios [b], P. Chouciño [a], E. Fraile-Nuez [b], R. Graña [a], M. Piedeleu [c], A. Rodríguez-Santana [c]

[a] Departamento de Ecoloxía e Bioloxía Animal, Universidade de Vigo, Vigo, Pontevedra 36200, Spain
[b] Instituto Español de Oceanografía, Centro Oceanográfico de Canarias, Santa Cruz de Tenerife 38180, Spain
[c] Departamento de Física, Universidad de Las Palmas de Gran Canaria, Las Palmas de Gran Canaria 35017, Spain

ABSTRACT

Measurements of microstructure turbulence were carried out, in the upper 300 m, in the tropical and subtropical Atlantic and Pacific oceans during the Malaspina 2010 expedition, by using a microstructure turbulence (MSS) profiler. Diapycnal diffusivity (K_ρ) was estimated from dissipation rates of turbulent kinetic energy (ε) measured by the MSS profiler, and also from hydrographic and meteorological data by using the K-profile parameterization (KPP). In the mixing layer, averaged K_ρ (169×10^{-4} m^2 s^{-1}) and ε (16.8×10^{-8} W kg^{-1}) were three and one orders of magnitude higher, respectively, compared to the ocean interior (0.59×10^{-4} m^2 s^{-1} and 1.0×10^{-8} W kg^{-1}). In general, the KPP showed a good agreement with diffusivity estimates derived from microstructure observations, both in the mixing layer and in the ocean interior. The KPP also reproduced the main regional patterns observed in the ocean interior. The analysis of turbulence generation mechanisms below the mixing layer showed that shear-induced mixing was more important in those regions influenced by the equatorial undercurrent, where averaged diffusivity was 2.27–3.62 $\times 10^{-4}$ m^2 s^{-1}. Favorable conditions for salt fingers formation were more frequently observed in the Atlantic, where, as a consequence of this process, diffusivity could increase up to 20%. This result could have important implications for the transport of heat and dissolved substances in these regions.

© 2014 Elsevier Ltd. All rights reserved.

1. Introduction

Turbulence plays a crucial role in ocean dynamics and global biogeochemical cycles through the redistribution of heat, salt and nutrients across isodensity surfaces (Thorpe, 2004). Diapycnal turbulent diffusion is essential to maintain ocean stratification and the meridional overturning circulation (Munk, 1966; Wunsch and Ferrari, 2004). Vertical diffusion of nitrate represents one of the main pathways of new nitrogen supply into the euphotic layer over large extensions of the open ocean (Mourino–Carballido et al., 2011). Moreover, turbulence through nutrient supply controls the taxonomic composition and the size–structure of plankton communities (Chisholm, 1992), which in turn determines the efficiency of the biological carbon pump (Falkowski and Oliver, 2007).

Several mechanisms are responsible for the generation of turbulence in the ocean. In the surface layer, turbulence is generated due to the interaction with the atmosphere by the exchange of density through heat and freshwater fluxes, the transfer of momentum through wind stress (Moum and Smyth, 2001), as well as by wave processes resulting in Langmuir turbulence (Belcher et al., 2012). In the stratified ocean interior, turbulence generation mechanisms include double diffusive and mechanical processes, such as shear instability and internal waves. Double diffusion occurs, under stable stratification conditions, as diffusive convection or salt fingers, when temperature or salinity profiles are unstable. Salt fingering is relevant in tropical and subtropical central waters, where warm and salty layers overlie cooler and fresher waters (Schmitt, 1981). Shear instability develops in stratified flows when vertical velocity shear overcomes the stabilizing effect of the buoyancy gradient. This process commonly happens in regions characterized by relatively strong shear induced by currents, as for example the equatorial domains (Moum et al., 1986; Gargett, 1989). Finally, mixing in stratified regions away from boundaries, where double diffusion is not important, is considered to be primarily driven by unresolved internal-waves shear (Munk and Wunsch, 1998).

Due to methodological limitations, microstructure turbulence has been extremely difficult to measure in the past. Although the

* Corresponding author.
E-mail address: bieito.fernandez@uvigo.es (B. Fernández-Castro).

use of free-falling microstructure profilers has become more common in the last few years, our current knowledge of the magnitude and global distribution of turbulence in the ocean is still scarce. A limited number of microstructure measurements carried out in the open ocean during the last 30 years of the 20th century were compiled by Gregg (1998). In more recent years, a few studies have been conducted across long distances in the Atlantic (Mourino–Carballido et al., 2011; Jurado et al., 2012b, 2012a), Arctic (Rainville and Winsor, 2008) and Pacific oceans (Gregg et al., 2003; Hibiya et al., 2007), and also the Mediterranean Sea (Cuypers et al., 2012). Microstructure profilers have been more frequently used to characterize the distribution of diffusivity in different parts of the ocean. However, these instruments have also been applied to calculate the oxygen supply in oxygen minimum zones (Fischer et al., 2013), the vertical flux of nitrate into the photic layer (Lewis et al., 1986; Hamilton et al., 1989; Sharples et al., 2009; Schafstall et al., 2010; Mourino–Carballido et al., 2011; Arcos-Pulido et al., 2014), and to study the influence of small-scale turbulence on the vertical distribution of plankton (Kunze et al., 2006a; Maar et al., 2003; Doubell et al., 2012).

Because of the scarcity of turbulence observations, a number of parameterizations have been developed during the last 20 years to estimate the vertical diffusivity and the contribution of different mechanisms to mixing. Internal waves interaction theories have been used to predict energy transfer through the vertical wavenumber spectrum towards small scales and turbulence production (Henyey et al., 1986). This parameterization, in the form proposed by Gregg (1989), has been frequently applied to estimate turbulent mixing and nutrient fluxes from finescale measurements of hydrography and currents (Gregg et al., 2003; Dietze et al., 2004; Kunze et al., 2006b; Cuypers et al., 2012). Several parameterizations have also been proposed for shear instability (Pacanowski and Philander, 1981; Jackson et al., 2008) and double diffusive processes (Schmitt, 1981; Kelley, 1990). The K-profile parameterization (KPP) proposed by Large et al. (1994), and frequently used in ocean models (Haidvogel et al., 2008), parameterizes the upper boundary layer based on the Monin–Obukhov similarity theory. For the ocean interior the KPP includes the contribution of shear instability, internal waves and double diffusion to mixing.

Measurements of microstructure turbulence collected during the Malaspina 2010 expedition, which sampled large areas in the main tropical and subtropical oceans, represent a unique opportunity to study the large-scale distribution of mixing. Here we analyze this dataset in order to (1) describe regional patterns of dissipation rates of

turbulent kinetic energy (ε) and diapycnal diffusivity (K_ρ), (2) study the regional variability in the mechanisms responsible for the generation of turbulence, and (3) verify the performance of the KPP parameterization under different hydrographical conditions.

2. Methods

Field observations were carried out mainly in the tropical and subtropical Atlantic, Indian and Pacific oceans between 14th December 2010 and 14th July 2011 during the Malaspina 2010 circumnavigation expedition on board R/V Hespérides. The cruise was divided into 7 legs: leg 1 (14th December 2010, Cádiz–13th January 2011, Rio de Janeiro), leg 2 (17th January, Rio de Janeiro–6th February, Cape Town), leg 3 (11th February, Cape Town–13th March, Perth), leg 4 (17th March, Perth–30th March, Sidney), leg 5 (16th April, Auckland–8th May, Honolulu), leg 6 (13th May, Honolulu–10th June, Cartagena de Indias), and leg 7 (19th June, Cartagena de Indias–14th July, Cartagena) (see Fig. 1).

2.1. Hydrography and currents

During the Malaspina expedition 147 Conductivity–Temperature–Depth (CTD) casts were carried out with a SBE911plus (Sea-Bird Electronics) probe attached to a rosette equipped with Niskin bottles, down to a depth of 4000 m. All CTD sensors were calibrated before the expedition. Horizontal currents were measured in 128 of these stations using a Lowered Acoustic Doppler Current Profiler (LADCP) system mounted on the rosette. The LADCP consists of two 300 kHz Teledyne/RDI Workhorses run in master/slave mode. The LADCP data were processed using the software developed by Fischer and Visbeck (1993), and provided current profiles with a vertical resolution of 10 m.

2.2. Dissipation rates of turbulent kinetic energy and thermal variance

Measurements of dissipation rates of turbulent kinetic energy (ε) were conducted at 50 stations by using a microstructure turbulence profiler (MSS, Prandke and Stips, 1998), down to a maximum depth of 300 m. 2–6 profiles were deployed at each station, resulting in a total number of 266 (see Table 1 in the Supplementary Material). The profiler was equipped with two microstructure shear sensors (type PNS06), a microstructure temperature sensor (FP07), a high-precision CTD probe and also
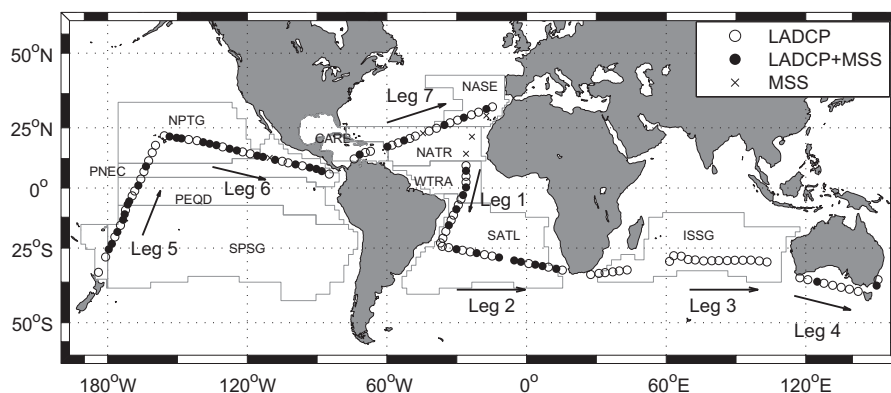

Fig. 1. Location of the Lowered Acoustic Doppler Current Profiler (LADCP, white circles) and microstructure turbulence profiler (MSS, crosses) stations carried out during the Malaspina expedition. Black circles indicate those stations where both LADCP and MSS equipments were deployed. Leg 1 (14th December 2010, Cádiz–13th January 2011, Rio de Janeiro), leg 2 (17th January, Rio de Janeiro–6th February, Cape Town), leg 3 (11th February, Cape Town–13th March, Perth), leg 4 (17th March, Perth–30th March, Sidney), leg 5 (16th April, Auckland–8th May, Honolulu), leg 6 (13th May, Honolulu–10th June, Cartagena de Indias) and leg 7 (19th June, Cartagena de Indias–14th July, Cartagena). Main biogeographical provinces crossed during the expedition, according to (Longhurst, 2006), are shown in the map: NASE (NE Atlantic Subtropical Gyral), NATR (North Atlantic Tropical Gyral), WTRA (Western Tropical Atlantic), SATL (South Atlantic Gyral), SPSG (South Pacific Subtropical Gyre), PEQD (Pacific Equatorial Divergence), PNEC (North Pacific Equatorial Countercurrent), NPTG (North Pacific Tropical Gyre), CARB (Caribbean) and ISSG (Indian South Subtropical Gyre).

a sensor to measure the horizontal acceleration of the profiler. The frequency of data sampling was 1024 Hz. The profiler was carefully balanced to have negative buoyancy in the water column and a sinking velocity of ~0.4–0.7 m s^{-1}. The shear sensors were calibrated before the cruise and the sensitivity was checked after each cast during the data processing. Due to technical problems, only one of the two shear sensors was properly working during the second part of leg 2 (stations 37–43) (see below). At the end of this leg, the equipment was taken ashore for repair and as a result, no microstructure turbulence data are available for leg 3.

Due to significant turbulence generation close to the ship, the data were considered to be reliable below 10 m. ε was computed in 512 data point segments, with 50% overlap, from the shear variance under the assumption of isotropic turbulence using the following equation:

$$\varepsilon = 7.5\nu \left\langle \left(\frac{\partial u}{\partial z}\right)^2 \right\rangle \text{(W kg}^{-1}) \quad (1)$$

where ν is the kinematic viscosity of seawater, $\partial u/\partial z$ the vertical shear and $\langle \cdot \rangle$ represents the ensemble average. The shear variance was computed by integrating the shear power spectrum. The lower integration limit was determined considering the size of the bins, and set to 2 cpm. The upper cut-off wavenumber for the integration of the shear spectrum was set as the Kolmogoroff number ($k_c = 1/(2\pi) \cdot (\varepsilon/\nu^3)^{1/4}$ cpm). An iterative procedure was applied to determine k_c. The maximum upper cut-off was not allowed to exceed 30 cpm to avoid the noisy part of the spectrum. Assuming a universal form of the shear spectrum, ε was corrected

for the loss of variance below and above the used integration limits, using the polynomial functions reported by Prandke et al. (2000). ε values were then averaged in 1 m bins. Peaks due to particle collisions were removed by comparing the dissipation rates computed simultaneously from the two shear sensors.

Fig. 2 shows shear power spectra for different dissipation rates spanning the range of the observed values. In general, a good agreement with the theoretical Nasmyth spectrum was found for $\varepsilon > 10^{-9}$ W kg^{-1}. Below this level the empirical spectrum showed a flatter shape, in comparison with the theoretical spectrum, indicating the proximity to the noise level, in good agreement with previous reports (Fischer, 2011). We calculated that the consideration of ε values below the detection limit of the MSS profiler (ca. 10^{-9} W kg^{-1}) overestimated station averages by about 8%, although the overestimation mainly affected a few stations where dissipation was $< 5 \times 10^{-9}$ W kg^{-1}.

The dissipation rate of thermal variance (χ) was calculated by fitting the temperature gradient spectrum, computed in 512 data point segments, to the theoretical Kraichnan spectrum (Sanchez et al., 2011) in the noise free region (2–40 cpm). Previously, the microstructure temperature signal was smoothed by averaging over 20 data points, the gradient calculated, and then smoothed by repeating the average over 20 data points. Due to technical problems no χ estimates are available for leg 5.

2.3. Thorpe length scale, mixing and mixed layers

We used the Thorpe length scale (L_T, Thorpe, 1977) to estimate the length scale of turbulent overturns. The Thorpe length scale
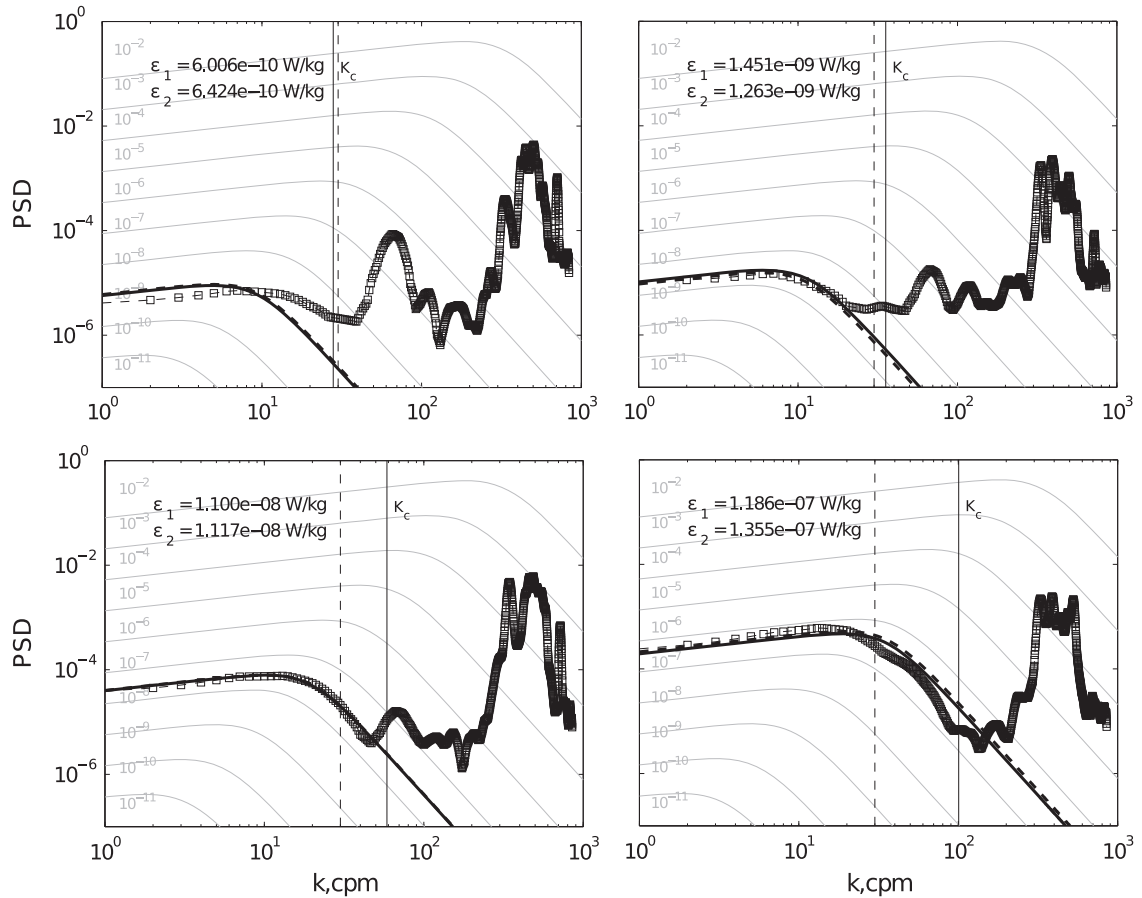

Fig. 2. Power spectral density (PSD) of microstructure shear for different levels of dissipation rates of turbulent kinetic energy ε. Empty squares represent the empirical spectrum. Two values of ε, in W kg^{-1}, are shown. The upper ε_1 was calculated from the iterative integration method, whereas ε_2 was obtained by least square fitting to the theoretical Nasmyth spectrum. Black thick continuous and dashed lines represent the theoretical spectra corresponding to ε_1 and ε_2 values, respectively. The Kolmogoroff wavelength (k_c) corresponding to ε_1 is indicated by the continuous vertical lines. Dashed vertical lines indicate the upper limit for integration and fitting (30 cpm).

was calculated in 1 m bins as the root mean square of the Thorpe displacements, computed after resorting the potential density profile in order to obtain static stability. L_T was calculated using the standard CTD sensors included in the MSS profiler. Following Brainerd and Gregg (1995), the mixing layer depth, noted as *mld*, was estimated as the deepest depth where surface and subsurface overturns penetrate. The mixed layer depth, noted in capitals as MLD, was calculated as the depth where local potential density exceeded by 0.1 kg m^{-3} the value of the shallowest data point.

2.4. Vertical diffusivity

Diapycnal diffusivity (K_ρ) was calculated using the popular Osborn (1980) 'dissipation method'. This model is derived from the turbulent kinetic energy equation, assuming that energy production is balanced by the sum of the work done against buoyancy and dissipation, neglecting the advective term and considering stationary state:

$$K_\rho = \Gamma \frac{\varepsilon}{N^2} \text{ (m}^2 \text{ s}^{-1}), \qquad (2)$$

where N^2 (s^{-2}) is the squared buoyancy frequency, and Γ is the mixing efficiency, derived from the flux Richardson number (R_f) as $\Gamma = R_f/(1-R_f)$, where R_f is the proportion of turbulent kinetic energy generated by shear that is transferred to potential energy through buoyancy flux (Dunckley et al., 2012). An additional assumption of the Osborn (1980) model is that $\Gamma = 0.2$ is constant (Oakey, 1982). Recent studies have questioned this assumption (Barry et al., 2001; Smyth et al., 2001; Shih et al., 2005; Ivey et al., 2008; Lozovatsky and Fernando, 2013), and parameterizations for Γ have been proposed as a function of the gradient Richardson number ($Ri = N^2/S^2$, where S is the vertical shear, e.g. Lozovatsky et al., 2006; Mellor and Yamada, 1982), the turbulence intensity parameter ($Re_b = \varepsilon/\nu N^2$, e.g. Shih et al., 2005), and other turbulent quantities (Ivey and Imberger, 1991). These parameterizations generally predict a decrease in the mixing efficiency for strong turbulence (decreasing Ri and/or increasing Re_b). At the present, an open debate exists about the applicability of these parameterizations (Kunze, 2011; Gregg et al., 2012). For this reason, we followed the traditional Osborn (1980) formulation, and we included a discussion about the implications of this choice (see Section 4.3), based on the comparison with the recently proposed Bouffard and Boegman (2013) (SKIF-B) parameterization.

The SKIF-B model prescribes four different turbulence regimes based on the Re_b parameter with the corresponding mixing efficiency (Γ_{SKIF-B}):

$$\Gamma_{SKIF-B} = 0, \quad Re_b < 1.7 \quad \text{Molecular} \qquad (3)$$

$$\Gamma_{SKIF-B} = 0.0615(Re_b)^{1/2}, \quad 1.7 < Re_b < 8.5 \quad \text{Buoyancy-Controlled} \qquad (4)$$

$$\Gamma_{SKIF-B} = 0.2, \quad 8.5 < Re_b < 100 \quad \text{Transitional} \qquad (5)$$

$$\Gamma_{SKIF-B} = 2(Re_b)^{-1/2}, \quad Re_b > 100 \quad \text{Energetic} \qquad (6)$$

In the particular case of the molecular regime the diffusion coefficient converges to the molecular value $K_\rho \sim 10^{-7}$ m^2 s^{-1}. The traditional mixing efficiency of 0.2, proposed by Osborn (1980), is only valid in the transitional regime.

In order to investigate the potential mixing caused by salt fingers we followed the weighting model proposed by St. Laurent and Schmitt (1999). According to St. Laurent and Schmitt (1999), averaged diffusivity can be modelled as the weighed sum of diffusivity due to turbulence (K^t) and salt fingers (K^{sf}), as $K^{tf} = P^{sf}K^{sf} + (1-P^{sf})K^t$, where P^{sf} is the weighting factor, corresponding to the fraction of bins where salt fingers are active. Favorable stratification for salt fingers can be

identified using the density ratio ($R_\rho = \alpha \partial_z T/\beta \partial_z S$, where α and β are the thermal expansion and salinity contraction coefficients, respectively). Although salt fingers are theoretically possible for $R_\rho > 1$, its contribution to mixing has been shown to be irrelevant for $R_\rho > 2$ (St. Laurent and Schmitt, 1999). According to McDougall (1988) and Hamilton et al. (1989), who solved the turbulent kinetic energy equation for salt fingers, mixing efficiency for this process is expected to exceed the value for mechanical turbulence of 0.2. Hence, we used two parameters to identify salt finger active bins, the density ratio ($1 < R_\rho < 2$) and the observed mixing efficiency ($\Gamma_{Obs} > 0.2$), calculated as $\Gamma_{Obs} = 0.5N^2\chi/\varepsilon(\partial_z T)^2$. Diffusivities for turbulence (K^t) and salt fingers (K^{sf}) bins were computed following the Osborn (1980), $K^t = \langle 0.2\varepsilon/N^2 \rangle^t$, and the Osborn and Cox (1972) models, $K^{sf} = \langle 0.5\chi/(\partial_z T)^2 \rangle^{sf}$, respectively. The Osborn and Cox (1972) model applies for heat. For dissolved substances $K_S^{sf} = rR_\rho^{-1}K^{sf}$, where $r = 0.4$–0.7 according to the compilation of estimates carried out by St. Laurent and Schmitt (1999), and here set to $r = 0.7$ for coherence with the K-profile parameterization (see below).

The vertical gradients of temperature ($\partial_z T$), salinity ($\partial_z S$) and potential density (N^2) were calculated by linearly fitting the profiles of the corresponding variable, obtained from the CTD included in the MSS profiler, in 10 m bins.
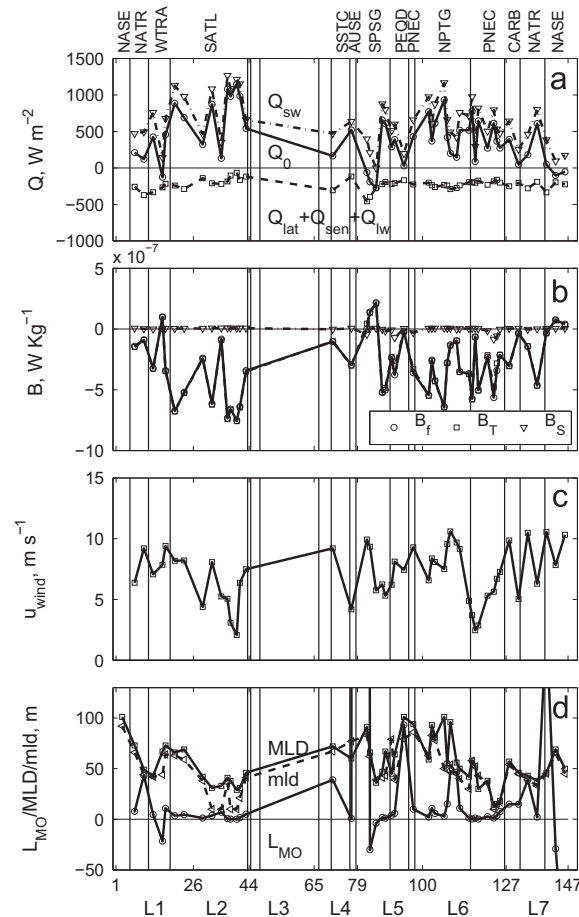

Fig. 3. (a) Mean surface heat fluxes (Q), (b) buoyancy fluxes (B), (c) wind speed (u_{wind}), and (d) mixed layer depth (MLD), mixing layer depth (*mld*) and Monin–Obukhov length scale (L_{MO}) computed at each station where the MSS profiler was deployed. Q_{sw}, Q_{lat}, Q_{sen}, Q_{lw}, Q_0, are the shortwave, latent, sensible, longwave and total heat fluxes, respectively. B_T and B_S are the buoyancy fluxes due to heat and freshwater, respectively, and B_f the total buoyancy flux. Biogeographical provinces crossed during the Malaspina expedition are indicated at the top axis and separated with vertical lines (see text for details). Numbers at the bottom correspond to station numbers. The first station of each leg (L) is indicated.

2.5. Meteorological data

Meteorological data were used to characterize the atmospheric forcing in the upper layer during the MSS profiler deployment (see Fig. 3 and Table 1 in the Supplementary Material), and also to calculate diffusivity in the boundary layer using the K-profile parameterization. Air temperature, air pressure, humidity, wind speed and direction, and irradiance were measured by the on-board Aanderaa meteorological station. Sea surface temperature and salinity data were collected using a SBE-21 thermosalinometer at a nominal depth of 3 m. These data were averaged during the duration of the MSS profiler (30–50 min) and LADCP deployments (about 4 h). Cloud cover and precipitation data were interpolated from the National Centers for Environmental Prediction (NCEP) reanalysis database for the time and location of the MSS and LADCP stations. The calculation of wind stress (τ_0), as well as latent (Q_{lat}), sensible (Q_{sen}) and longwave (Q_{lw}) heat fluxes was performed using the Matlab Air-Sea toolbox (version 2.0, http://sea-mat.whoi.edu). Net turbulent heat flux (Q_t) was calculated as the sum of the latent, sensible and longwave heat fluxes. Net heat flux (Q_0) was computed as the sum of the net turbulent heat flux and the solar irradiance (I or shortwave heat flux, Q_{sw}). Freshwater flux (F_t) was computed as the excess of precipitation (P) over evaporation (E), where $E = Q_{lat}/l_E$ and $l_E = 2.5 \times 10^6$ J kg^{-1} is the latent heat of evaporation.

Surface kinematic heat ($\overline{wt}_0$), salt ($\overline{ws}_0$) and buoyancy fluxes ($\overline{wb}_0$) were computed, respectively, as

$$\overline{wt}_0 = -Q_t/(\rho_0 C_{p0}) \tag{7}$$

$$\overline{ws}_0 = F_t S_0/\rho_0(0) \tag{8}$$

$$\overline{wb}_0 = g(\alpha \overline{wt}_0 - \beta \overline{ws}_0) \tag{9}$$

where ρ_0, $C_{p\ 0}$ and S_0 are the density, specific heat and salinity, respectively, at the surface reference pressure. $\rho_0(0)$ is the density at the surface reference pressure and $S_0 = 0$, and $g = 9.81$ m s^{-2} is the gravity acceleration.

The buoyancy profile ($B(z)$, W kg^{-1}) and the buoyancy forcing (B_f, W kg^{-1}) were computed as:

$$B(z) = g(\alpha T - \beta S) \tag{10}$$

$$B_f = -\overline{wb}_0 + B_R \tag{11}$$

where $B_R = g[(\alpha I/\rho C_p)_{z=0} - (\alpha I/\rho C_p)_{z=h}]$, and the subscripts 0 and h refer to the surface and the boundary layer depth (see supplementary material), respectively. $I = I(d)$ (W m^{-2}) is the vertical distribution of solar irradiance in the water column computed for a Jerlov water type I, suitable for open ocean clear waters, following Paulson and Simpson (1977). For the calculations corresponding to the MSS profiler data, as the boundary layer depth was unknown, we assumed that $I(h) \sim 0$.

The friction velocity (u^*) and the Monin–Obukhov length-scale (L_{MO}) were computed as

$$u^{*2} = \tau_0/\rho_0 \tag{12}$$

$$L_{MO} = -u^{*3}/(\kappa B_f) \tag{13}$$

where τ_0 is the wind stress and $\kappa = 0.4$ is the von Kármán constant. $L_{MO} > 0$ (< 0) indicates convectively stable (unstable) conditions in the upper ocean.

2.6. K-profile parameterization

The K-profile parameterization (KPP) described by Large et al. (1994) was used to compute vertical diffusivity of temperature (K_T, see the Supplementary Material) at 128 stations where LADCP, CTD and meteorological data were available. According to this model the water column is divided into the upper boundary layer, where wind stress and buoyancy fluxes are the mechanisms responsible for the mixing, and the lower ocean interior where mixing is produced by shear instability, internal waves and double diffusion. Parameterization of diffusivity in the boundary layer is based on the Monin–Obukhov similarity theory and computed using the calculated buoyancy and momentum atmospheric fluxes. Shear instability parameterization was based on the gradient Richardson number ($Ri = N^2/S^2$), where N^2 is the buoyancy frequency computed from CTD measurements, and S^2 is the squared vertical shear of the horizontal velocities derived from LADCP measurements. Internal waves diffusivity was set to a background value of 10^{-5} m^2 s^{-1}. The formulation of salt fingers diffusivity was based on the density ratio (R_ρ). The parameterization was implemented in a uniform 10 m grid constrained by the vertical resolution of the LADCP profiler. Only the implementation for temperature (K_T) is reported in this paper. A complete description of the implemented parameterization is given in the Supplementary Material.

3. Results

3.1. Hydrographical properties

Fig. 4 shows the vertical distribution of temperature, buoyancy frequency and vertical shear during the Malaspina expedition. Biogeographical provinces according to the classification carried out by Longhurst (2006) were used to describe the geographical distribution of properties. This classification was chosen to facilitate the comparison with complementary studies carried out during the multidisciplinary Malaspina 2010 Expedition.

Leg 1 crossed the NE Atlantic Subtropical Gyral (NASE), the North Atlantic Tropical Gyral (NATR), the Western Tropical Atlantic (WTRA) and the South Atlantic Gyral (SATL) biogeographical provinces. The influence of the equatorial upwelling in some stations sampled at NATR and WTRA was noticed by the shoaling of the 16 °C isotherm above 200 m, reflecting the upwelling of deeper waters. The vertically averaged temperature in the mixed-layer ($\langle T \rangle_{ML}$) was lower in NASE compared to the other three provinces sampled during this leg. The stratification in the seasonal pycnocline (N_{max}) was higher in the tropical (NATR, WTRA) compared to the subtropical (NASE, SATL) provinces. Higher values of shear (ca. 0.0082 s^{-1}) were observed in WTRA at station 16 (0.21°N–26.02°W).

Most stations during leg 2 sampled a zonal transect across the South Atlantic Gyral (SATL) province, the last station being carried out in the Benguela Current Coastal (BENG) province. This leg was characterized by an eastward decrease in $\langle T \rangle_{ML}$, and an increase in surface stratification.

Leg 3 crossed the Indian ocean from west to east. The first three stations were carried out in the East Africa Coastal (EARF) province, whereas most of the stations sampled the Indian South Subtropical Gyre (ISSG) province.

Four provinces were sampled along the South Australian coast during leg 4: ISSG, the Australia–Indonesia Coastal (AUSW), the South Subropical Convergence (SSTC) and the East Australia Coastal (AUSE) provinces. The lowest value of $\langle T \rangle_{ML}$ recorded during the expedition (ca. 16.7 °C) was measured in those stations sampled in SSTC.

During leg 5 the South Pacific Subtropical Gyre (SPSG), the Equatorial Pacific (PEQD), the North Pacific Equatorial Countercurrent (PNEC) and the North Pacific Tropical Gyre (NPTG) provinces were sampled. A progressive increase in $\langle T \rangle_{ML}$ was observed as travelling northward in SPSG. Afterwards a decrease in $\langle T \rangle_{ML}$ was observed when crossing PEQD, PNEC and NPTG.
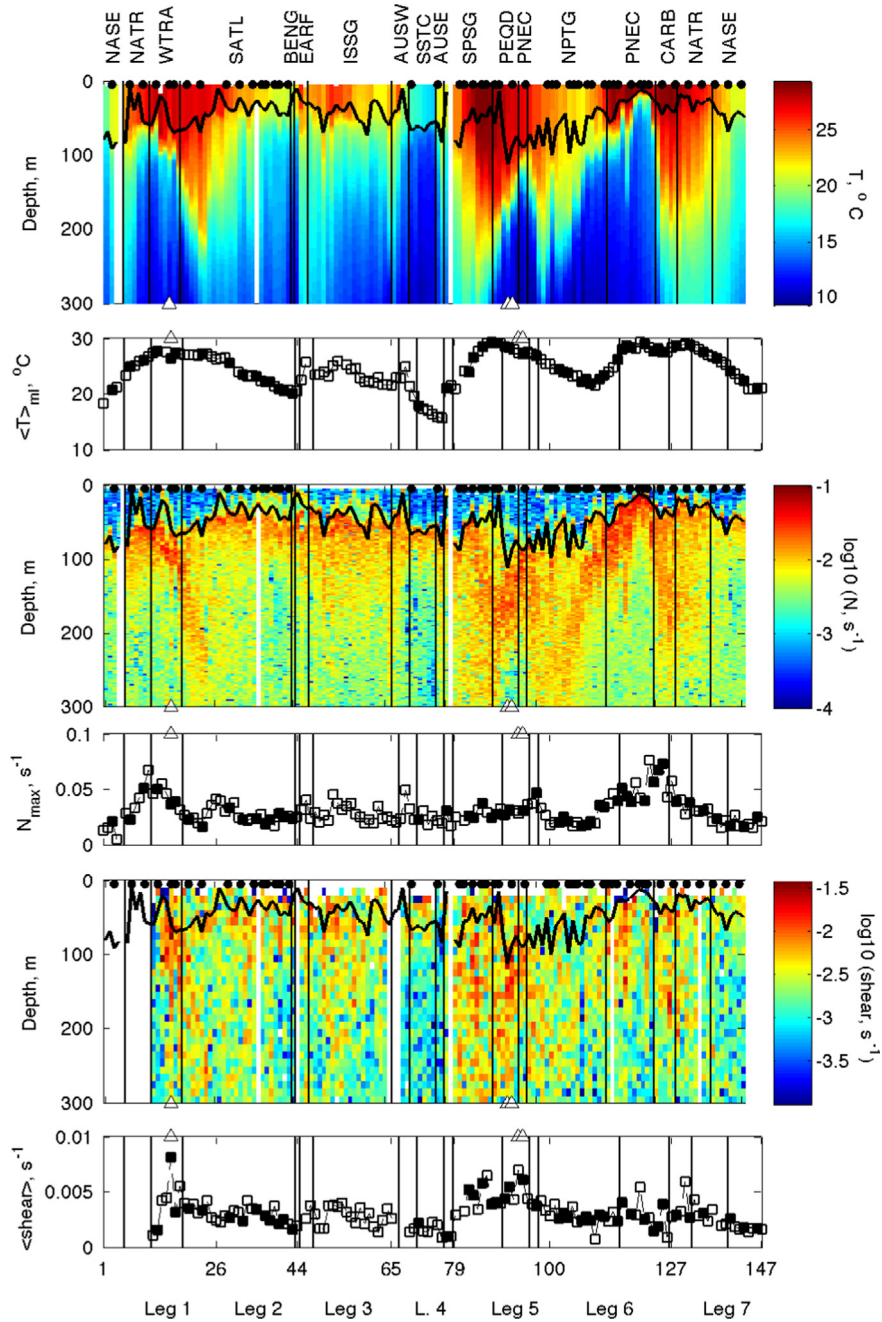
Fig. 4. Vertical distribution of temperature (T), buoyancy frequency (N) and velocity shear during the Malaspina expedition. Averaged temperature in the mixed layer ($\langle T \rangle_{ML}$), maximum stratification (N_{max}) and averaged shear in the upper 300 m are also included. Black dots at the top axes and black filled squares in the lower panels indicate the stations where MSS deployments were conducted. The black line represents the mixed layer depth (0.1 kg m^{-3} density difference respect to the shallowest data point). White triangles indicate stations sampled less than 2° away from the equator (stations 16, 93 and 94). Numbers at the bottom correspond to station numbers. The first station of each leg (L) is indicated. Biogeographical provinces crossed during the expedition are indicated at the top axis (see text for details).

Maximum values of shear (ca. 0.025 s^{-1}) measured at ca. 100 m in PEQD were related to the influence of the Equatorial Undercurrent (EUC).

The leg 6 crossed the North Pacific Tropical Gyre (NPTG) and again the PNEC province. $\langle T \rangle_{ML}$ first decreased as we travelled eastward in NPTG, but then it increased reaching maximum values of 30 °C in PNEC. In this province the depth of the mixed layer was relatively shallow (< 40 m) and N_{max} was enhanced (ca. 0.052 s^{-1}).

Finally, during leg 7 the Caribbean sea (CARB), NATR and NASE provinces were sampled. A progressive decrease in $\langle T \rangle_{ML}$ and N_{max} was observed when travelling from west to east.

3.2. Dissipation rates of turbulent kinetic energy and diapycnal diffusivity

In order to study the variability of dissipation rates of turbulent kinetic energy (ε) and diapycnal diffusivity (K_ρ) derived from the MSS profiler, we divided the water column into the upper mixing layer (ml) (see Section 2.3) and the deeper ocean interior (oi). Higher values of ε and K_ρ were observed in general in the mixing layer compared to the ocean interior (see Fig. 5). The vertical distribution of ε in the ocean interior was patchy, and the vertical structure of K_ρ, mainly determined by the buoyancy frequency (N), exhibited lower values in the seasonal pycnocline.
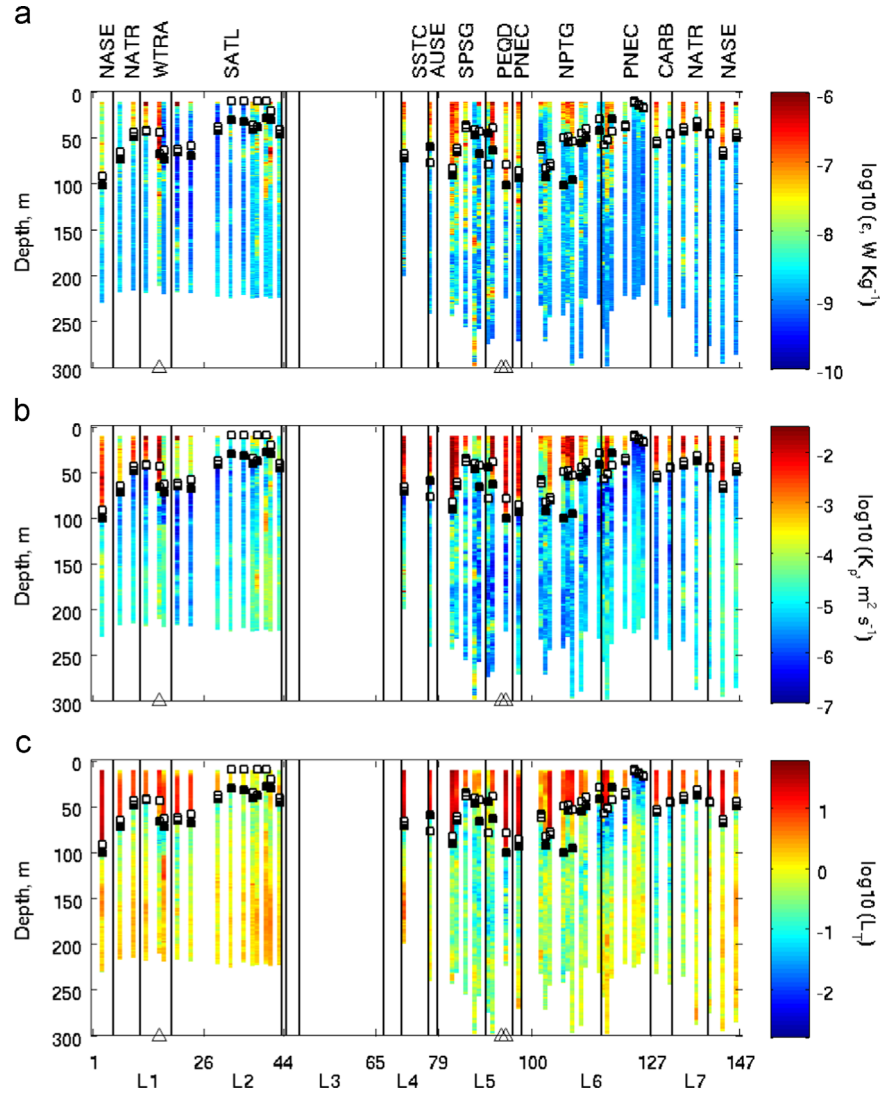
Fig. 5. Vertical distribution of averaged profiles of (a) dissipation rates of turbulent kinetic energy (ε, W kg^{-1}); (b) diapycnal diffusivity (K_ρ, m^2 s^{-1}); and (c) Thorpe length scale (L_T, m), derived from the MSS profiler during the Malaspina expedition. White triangles indicate stations sampled less than 2° away from the equator (stations 16, 93 and 94). White and black squares indicate the mixing and mixed layer depths (see Methods). Numbers at the bottom correspond to station numbers. The first station of each leg (L) is indicated. Biogeographical provinces crossed during the expedition are indicated (see text for details).
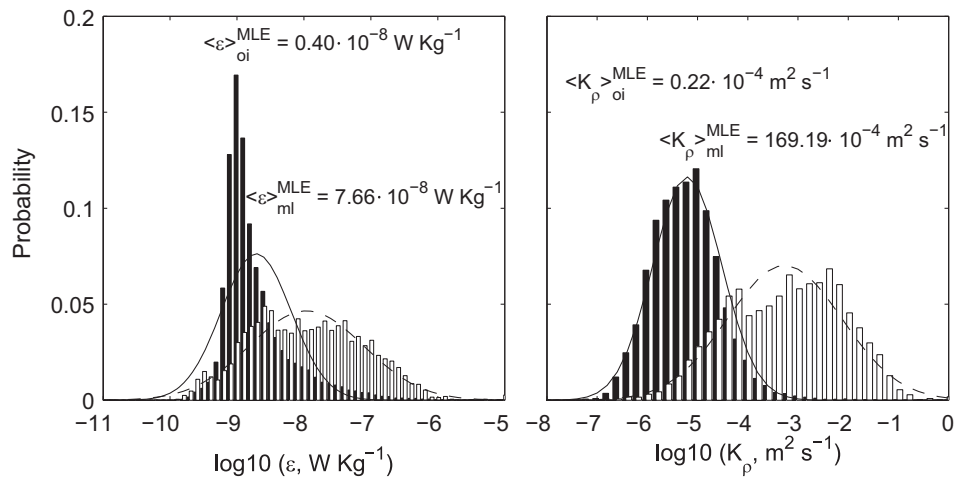

Fig. 6. Probability distribution of energy dissipation rate (ε, left), and diapycnal diffusivity (K_ρ, right), computed in the mixing layer (white bars) and the ocean interior (black bars). Continuous and discontinuous lines represent the log-normal probability distributions fitted to the experimental data. Those probabilities are plotted in area-preserving form, characterized by equal contributions to the mean from equal areas of the curve (Gregg, 1998).

The probability distributions of ε and K_ρ, computed using all the data collected in the mixing layer and the ocean interior, follow approximately a log-normal shape (see Fig. 6). Maximum likelihood estimates (MLE) for the mean values of ε and K_ρ (X) were computed following Baker and Gibson (1987):

$$\langle X \rangle^{MLE} = \exp(\mu + \tfrac{1}{2}\sigma^2) \qquad (14)$$

where μ and σ are the expected value and the standard deviation of $\ln X$, respectively. The distribution of ε in the mixing layer ranged from 10^{-10} to 10^{-6} W kg^{-1}. The fit to a log-normal distribution gave $\mu_{ml}^\varepsilon = -18.33$, $\sigma_{ml}^\varepsilon = 1.97$ and MLE $= 7.7[6.8-8.6] \times 10^{-8}$ W kg^{-1}, with the arithmetic mean being $16.8[5.3-37.6] \times 10^{-8}$ W kg^{-1} (95% confidence intervals obtained from bootstraping shown in brackets). The distribution of ε in the ocean interior was more peaked than a lognormal distribution, with around 80% of the values in the range 6.3×10^{-10} to 1×10^{-8} W kg^{-1}. The fit to a log-normal distribution gave $\mu_{oi}^\varepsilon = -20.06$, $\sigma_{oi}^\varepsilon = 1.20$, MLE $= 0.40[0.38-0.41] \times 10^{-8}$ W kg^{-1}, and the arithmetic mean $1.0[0.90-1.22] \times 10^{-8}$ W kg^{-1}.

The distribution of K_ρ in the mixing layer ranged from $\sim 10^{-6}$ m^2 s^{-1} to 10^{-1} m^2 s^{-1}. The log-normal fitting provided $\mu_{ml}^{K_\rho} = -7.52$, $\sigma_{ml}^{K_\rho} = 2.62$ in the typical range described by Gregg (1998), and MLE $= 169[152-193] \times 10^{-4}$ m^2 s^{-1}. The arithmetic mean was $262[130-586] \times 10^{-4}$ m^2 s^{-1}. In the ocean interior K_ρ distribution provided $\mu_{oi}^{K_\rho} = -11.98$, $\sigma_{oi}^{K_\rho} = 1.58$, MLE $= 0.217[0.211-0.225] \times 10^{-4}$ m^2 s^{-1}, and the arithmetic mean $0.59[0.49-0.75] \times 10^{-4}$ m^2 s^{-1}. On average, ε and K_ρ values in the mixing layer were one and three orders of magnitude higher, respectively, compared to the ocean interior.

In order to describe the regional variability of ε and K_ρ, station averages were computed for the mixing layer and the ocean interior. For coherence with the St. Laurent and Schmitt (1999) model (see Methods), and also following Davis (1996), arithmetic averages are reported next. The values of ε in the mixing layer ($\langle\varepsilon\rangle_{ml}$), which are influenced by local meteorological conditions, were subjected to an important regional variability ranging from 10^{-9} to 10^{-4} W kg^{-1} (Fig. 7), with 80% of the values lower than

10^{-7} W kg^{-1}. A clear regional pattern was not observed. No values are reported for some stations in SATL (stations 32, 35, 40) and PNEC (station 123), because no mixing layer was observed, as no significant overturns penetrated below 11 m according to the Thorpe lengthscale (L_T) (Fig. 5).

In the ocean interior ε estimates ranged between 1.1×10^{-9} and 9.9×10^{-8} W kg^1. Higher values ($> 5 \times 10^{-8}$ W kg^{-1}) were found in the stations 16 and 91, sampled in WTRA and PEQD, respectively, and at station 71 in the south coast of Australia. We cannot discard that the relatively high values observed in the eastern SATL (stations 40, 41) were, at least partially, influenced by the fact that only one of the two shear sensors was operating (see Methods). Lower values ($< 0.3 \times 10^{-8}$ W kg^{-1}) were sampled in the western SATL (stations 17, 23, 29, 37, 37), PNEC (stations 107, 108, 123, 125) and NASE (stations 140, 146).

Diffusivity in the mixing layer ($\langle K_\rho \rangle_{ml}$) ranged from 3×10^{-5} m^2 s^{-1} to 1.5 m^2 s^{-1} (see Fig. 8, and Table 2 in the Supplementary Material). Lower values were found in SATL (stations 29, 38, 43), NPTG (station 115) and PNEC (station 125), whereas higher values corresponded to WTRA (station 13), SATL (station 20), SPSG (station 82), PEQD (station 91) and NASE (station 146).

Diapycnal diffusivity in the ocean interior ($\langle K_\rho \rangle_{oi}$) ranged from 0.03 to 10×10^{-4} m^2 s^{-1}. Higher values corresponded to the station 16 in WTRA, stations 91 and 94 in PEQD, and station 71 in the south coast of Australia. Lower values of $\langle K_\rho \rangle_{oi} < 10^{-5}$ m^2 s^{-1} were found in the western SATL (stations 20, 23), SPSG (station 88), NPTG (stations 104, 108), PNEC (stations 112, 115, 121, 125) and CARB (stations 128, 131).

Averaged ε and K_ρ computed in the mixing layer and the ocean interior for the main biogeographical provinces sampled during the Malaspina expedition are shown in Table 1. The description in terms of provinces is more suitable for the ocean interior, which is less exposed to local meteorological conditions. Higher values of ε were computed for the Atlantic WTRA (2.3×10^{-8} W kg^{-1}), and the Pacific PEQD (2.8×10^{-8} W kg^{-1}) and SPSG (1.5×10^{-8} W kg^{-1}), whereas lower values were calculated for the Caribbean (CARB, 0.34×10^{-8} W kg^{-1}). Higher values of K_ρ were
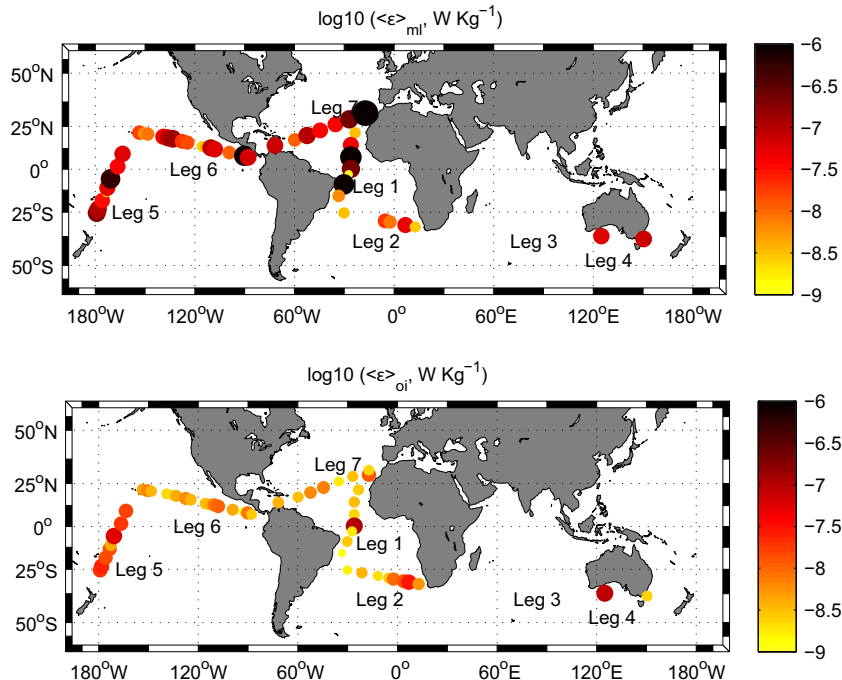

Fig. 7. Averages of dissipation rates of turbulent kinetic energy (ε, W kg^{-1}), computed for the mixing layer (ml) and the ocean interior (oi) at the stations sampled during the Malaspina expedition.

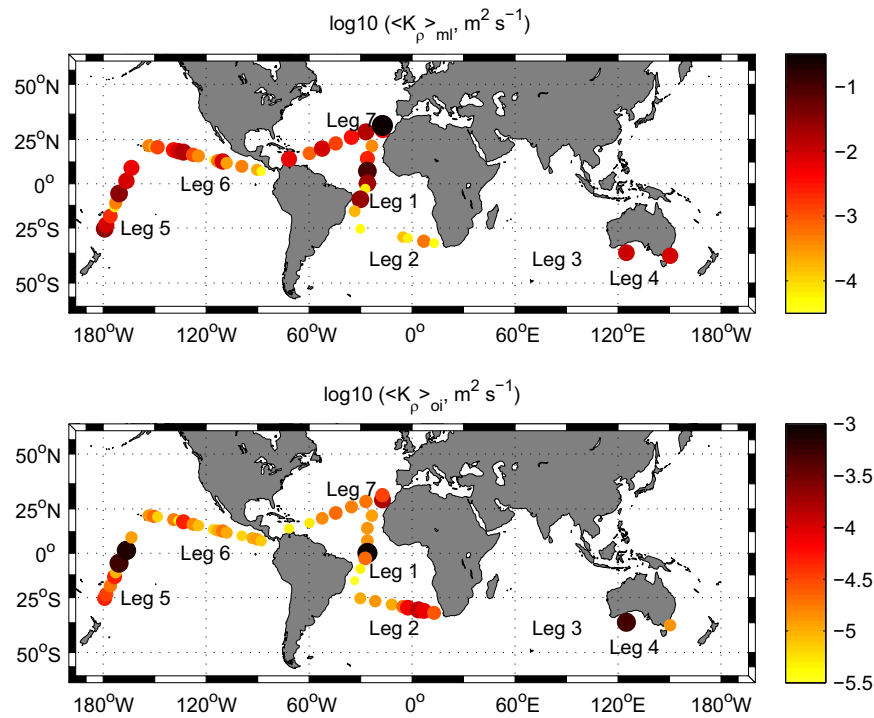**Fig. 8.** Averages of diapycnal diffusivity (K_ρ, m^2 s^{-1}), computed from microstructure observations for the mixing layer (*ml*) and the ocean interior (*oi*) at the stations sampled during the Malaspina expedition.

Table 1
Averages of dissipation rates of turbulent kinetic energy (ε) and diapycnal diffusivity (K_ρ) computed in the mixing layer (*ml*) and the ocean interior (*oi*) for the main biogeographical provinces sampled during the Malaspina expedition (Prov.). 95% confidence intervals are shown in brackets. NMSS is the number of MSS profiles conducted at each province.

Prov.	NMSS	$\langle\varepsilon\rangle_{ml}$ 10^{-8} (W kg^{-1})	$\langle\varepsilon\rangle_{oi}$ 10^{-8} (W kg^{-1})	$\langle K_\rho\rangle_{ml}$ 10^{-4} (m^2 s^{-1})	$\langle K_\rho\rangle_{oi}$ 10^{-4} (m^2 s^{-1})
NASE	12	1594 [382–4067]	0.44 [0.33–0.70]	1913 [679–4686]	0.461 [0.316–0.822]
NATR	12	4.0 [3.4–4.8]	0.54 [0.48–0.65]	28.3 [21.6–38.7]	0.159 [0.146–0.184]
WTRA	9	115 [43–349]	2.3 [1.6–3.2]	386 [144–1007]	2.27 [1.44–3.84]
SATL	35	27 [7–81]	0.86 [0.70–1.19]	64.9 [12.6–186.3]	0.433 [0.385–0.478]
CARB	7	5.0 [4.1–6.2]	0.34 [0.29–0.43]	39.1 [31.9–50.2]	0.050 [0.043–0.065]
SPSG	20	9.8 [8.8–11.5]	1.5 [1.3–1.7]	132 [112–151]	0.296 [0.266–0.330]
PEQD	11	8.7 [5.9–15.2]	2.8 [2.3–3.4]	74.6 [60.7–104.8]	3.62 [2.87–4.88]
PNEC	27	6.6 [5.6–8.4]	0.72 [0.61–0.97]	44.7 [39.8–52.8]	0.125 [0.119–0.135]
NPTG	29	3.9 [3.0–6.0]	0.43 [0.40–0.48]	39.3 [32.9–50.5]	0.170 [0.147–0.222]

also computed for WTRA (2.27×10^{-4} m^2 s^{-1}) and PEQD (3.62×10^{-4} m^2 s^{-1}), whereas lower values were computed for CARB (0.05×10^{-4} m^2 s^{-1}).

3.3. Parameterized vertical diffusivity

In order to verify the performance of the K-profile parameterization (KPP) under different hydrographical conditions, we used the model proposed by Large et al. (1994) (see Methods and the Supplementary Material). The vertical distribution of diffusivity computed by using the KPP (K_T) is shown in Fig. 9. Diffusivity values ranged from the lower level of 0.1×10^{-4} m^2 s^{-1}, determined by the background internal wave mixing, to 49×10^{-4} m^2 s^{-1} in the ocean interior, and 1800×10^{-4} m^2 s^{-1} in the boundary layer. The probability distribution of parameterized K_T did not show a lognormal shape, either in the boundary layer or in the ocean interior (data not shown). For this reason only arithmetic averages were used in this section. Averaged K_T in the boundary layer ($260[230-300] \times 10^{-4}$ m^2 s^{-1}, 95% confident

intervals between brackets) was in very good agreement with the diffusivity estimate derived from the microstructure profiler (262×10^{-4} m^2 s^{-1}). In the ocean interior averaged parameterized diffusivity ($0.61[0.51-0.74] \times 10^{-4}$ m^2 s^{-1}) was also in close agreement with the estimate derived from the microstructure profiler (0.59×10^{-4} m^2 s^{-1}).

Fig. 10 shows the comparison of averaged profiles of parameterized K_T and K_ρ derived from microstructure observations computed for the biogeographical provinces crossed during the expedition. The parameterization reproduces in general the shape of the K_ρ profiles. Note that both estimates were obtained from two different sets of stations what could explain part of the differences observed between the averaged vertical distributions. For example, no parameterized K_T was available for station 3, sampled in NASE during winter, where mixing layer extended down to 100 m (see Fig. 5).

Averaged parameterized K_T computed for the boundary layer and the ocean interior in the biogeographical provinces sampled during the expedition are shown in Table 2. Note that diffusivity
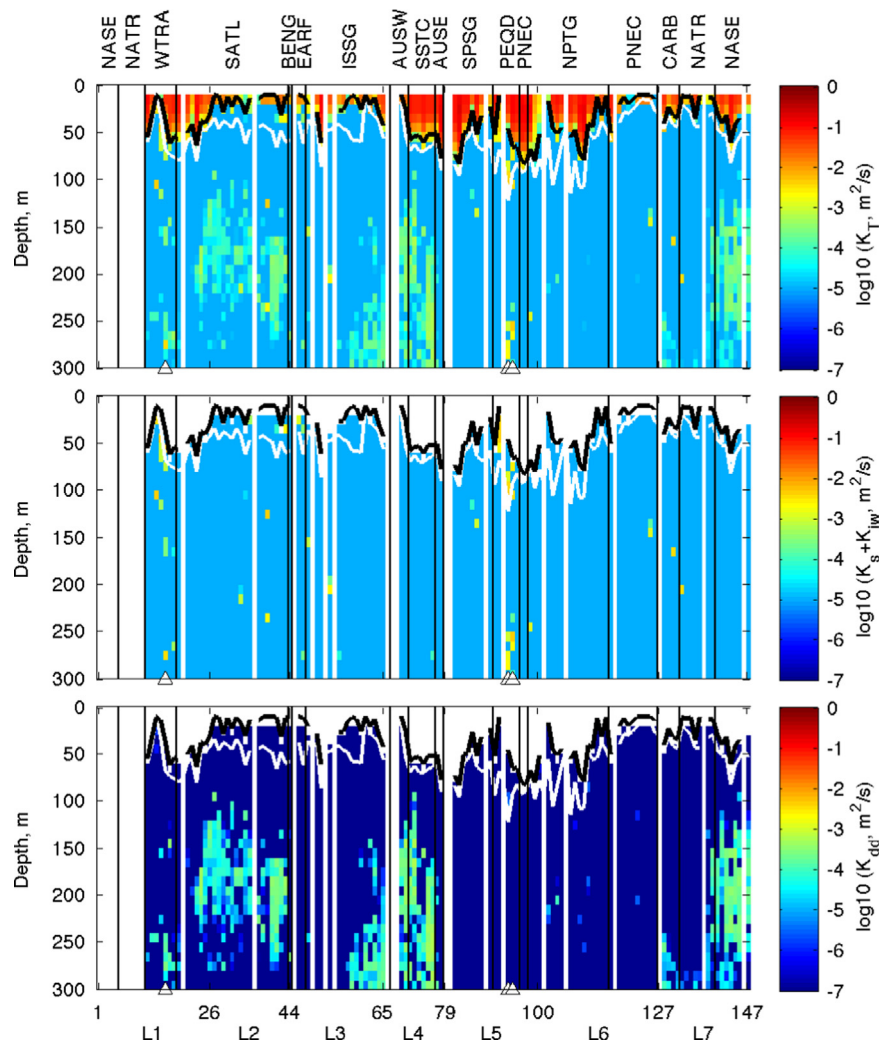
Fig. 9. Parameterized vertical temperature diffusivity (K_T, m^2 s^{-1}) computed along the Malaspina expedition. Shear instability plus internal waves ($K_s + K_{iw}$) and also double diffusion (K_{dd}) contributions are included. The black and white lines represent the boundary layer and the mixed layer depth, respectively. White triangles indicate stations sampled less than 2° away from the equator (stations 16, 93 and 94). Numbers at the bottom correspond to the station numbers. Biogeographical provinces crossed during the expedition are indicated (see text for details).

parameterization was computed in the Indian Subtropical Gyre (ISSG) where no microstructure observations were conducted (see Methods). In the ocean interior higher diffusivities were computed for the equatorial WTRA in the Atlantic (1.46×10^{-4} m^2 s^{-1}) and PEQD in the Pacific (3.7×10^{-4} m^2 s^{-1}), due to the influence of the Equatorial Undercurrent in the shear instability term (Fig. 9). Lower diffusivities (ca. 0.15×10^{-4} m^2 s^{-1}) were computed for the Pacific provinces NPTG, PNEC and SPSG. Salt fingers favorable stratification was frequently observed in the Atlantic subtropical provinces NASE and SATL, and in the Australian AUSW, where the contribution of this process to mixing was 0.73×10^{-4} m^2 s^{-1}, 0.24×10^{-4} m^2 s^{-1} and 0.96×10^{-4} m^2 s^{-1}, respectively.

4. Discussion

4.1. Turbulence generating mechanisms in the boundary layer

In the upper ocean layer, buoyancy fluxes and wind forcing represent the main mechanisms responsible for the generation of turbulence (Moum and Smyth, 2001). In order to investigate the contribution of these two processes we analyzed the meteorological conditions, at the time of sampling, during the expedition (see Fig. 3 and Table 1 in the Supplementary Material).

The total surface heat flux (Q_0) was always positive from the atmosphere to the ocean, except at stations 16, 82–85 and 143–146, indicating heat gain by the ocean as a result of the contributions of sensible (Q_{sen}), latent (Q_{lat}), longwave (Q_{lon}) and shortwave (Q_{sw}) heat fluxes. Sea surface temperature was always lower than air temperature, resulting in negative Q_{sen}. Q_{lat} and Q_{lw} were also negative in all the stations, whereas Q_{sw} was always positive, because the profiler was deployed during daylight. As a consequence, buoyancy fluxes (B_f) were always negative, indicating a gain in stability and resulting in positive Monin–Obukhov length scales (L_{MO}), except at stations 16, 83, 85, 143 and 146. This result indicates convectively stable conditions during the profiler deployment, pointing out to the wind forcing as the main turbulence generation mechanism in the boundary layer. However, L_{MO} was generally shallower than the mixed and mixing layer depths, indicating that wind forcing alone cannot explain all mixing in this layer, which could also be the result of previous convection episodes during the nighttime.

Similar conclusions can be obtained from observing the behavior of turbulent and mixing conditions in the upper layer (see Fig. 5). In general, the mixing layer depth, computed as the depth reached by significant overturning from the surface (see Methods), showed a good agreement with the layer where relatively enhanced ε and K_ρ were observed. However, the mixing layer
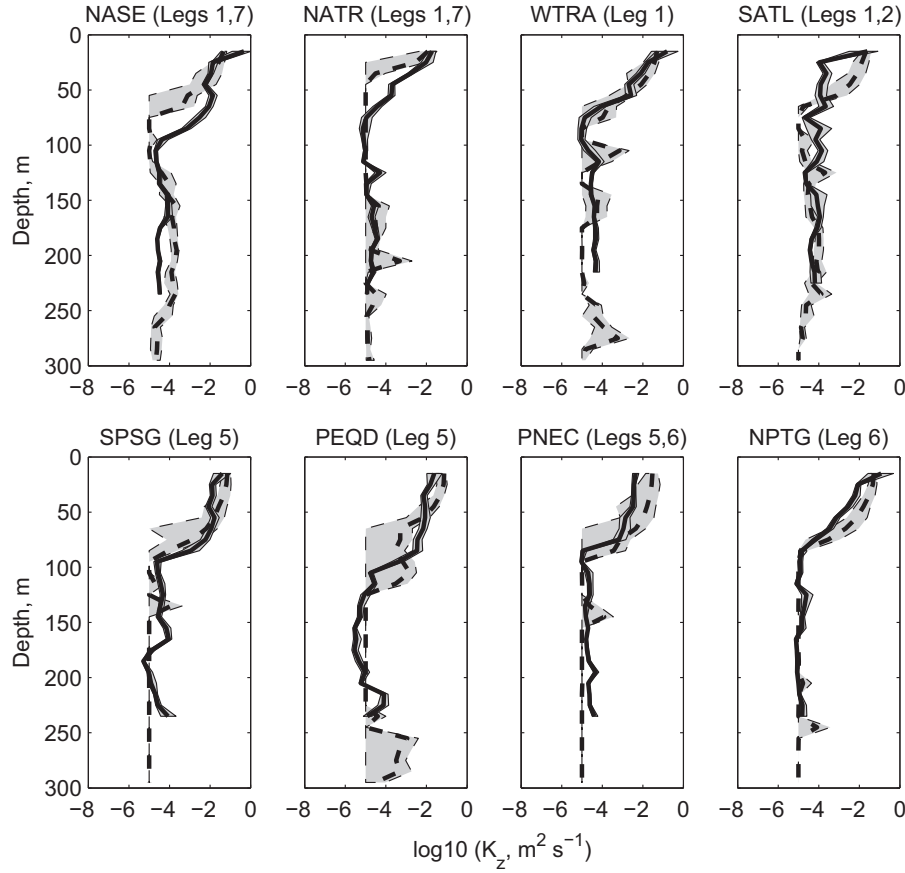
Fig. 10. Profiles of vertical temperature diffusivity computed using the KPP parameterization (K_T, dashed line) and diapycnal diffusivity (K_ρ) inferred from microstructure observations using the Osborn (1980) model (solid black line) for the biogeographical provinces sampled during the Malaspina expedition. Diapycnal diffusivity was averaged in 10 m bins to allow direct comparison with parameterized K_T. Shadowed areas represent 95% confidence intervals computed by using bootstraping.

Table 2
Averaged parameterized vertical temperature diffusivity (K_T) computed for the main biogeographical provinces (Prov.) explored during the Malaspina expedition. Total boundary layer ($\langle K_T \rangle_{bl}$) and ocean interior ($\langle K_T \rangle_{oi}$) diffusivities, and shear instability plus internal waves ($\langle K_s + K_{iw} \rangle_{oi}$) and double diffusion ($\langle K_{dd} \rangle_{oi}$) terms are shown. $\langle K_{loz} \rangle_{oi}$ is the diffusivity parameterized using the scaling as a function of the Richardson number, Ri (see Section 4.2). NKPP is the number of stations sampled at each province.

Prov.	NKPP	$\langle K_T \rangle_{ml}$ 10^4 (m² s⁻¹)	$\langle K_T \rangle_{oi}$	$\langle K_s + K_{iw} \rangle_{oi}$	$\langle K_{dd} \rangle_{oi}$	$\langle K_{loz} \rangle_{oi}$
NASE	7	207 [121–304]	0.83 [0.65–0.97]	0.10 [0.10–0.10]	0.73 [0.57–0.88]	0.30 [0.28–0.32]
NATR	7	64.6 [28.4–194.8]	0.33 [0.14–0.83]	0.27 [0.10–0.80]	0.05 [0.02–0.11]	0.31 [0.29–0.33]
WTRA	7	266 [176–424]	1.6 [0.7–3.3]	1.48 [0.83–3.06]	0.09 [0.05–0.17]	0.43 [0.39–0.49]
SATL	23	145 [103–218]	0.50 [0.38–0.79]	0.26 [0.16–0.52]	0.24 [0.20–0.29]	0.35 [0.33–0.36]
CARB	4	142 [65–244]	0.48 [0.13–1.48]	0.43 [0.10–1.74]	0.05[0.02–0.13]	0.29 [0.27–0.34]
SPSG	8	424 [313–607]	0.15 [0.10–0.33]	0.15 [0.10–0.28]	0.00 [0.00–0.00]	0.36 [0.34–0.39]
PEQD	5	410 [288–598]	3.7 [2.2–6.5]	3.65 [1.74–5.68]	0.00 [0.00–0.00]	0.51 [0.44–0.60]
PNEC	12	308 [186–459]	0.15 [0.11–0.41]	0.15 [0.11–0.32]	0.00 [0.00–0.00]	0.33 [0.31–0.35]
NPTG	16	292 [234–378]	0.13 [0.10–0.23]	0.13 [0.10–0.22]	0.00 [0.00–0.01]	0.28 [0.27–0.29]
EAFR	2	56.4 [7.7–113.0]	0.45 [0.18–1.20]	0.45 [0.16–1.26]	0.00 [0.00–0.00]	0.38 [0.33–0.47]
ISSG	15	134 [79–239]	0.29 [0.23–0.50]	0.17 [0.12–0.34]	0.11 [0.08–0.17]	0.32 [0.31–0.34]
AUSW	2	87.6 [25.5–176.7]	1.5 [0.9–3.7]	0.54 [0.10–1.56]	0.96 [0.67–1.49]	0.28 [0.26–0.36]
AUSE	2	562 [305–915]	0.15 [0.11–0.25]	0.10 [0.10–0.10]	0.05 [0.01–0.17]	0.23 [0.22–0.24]
SSTC	6	357 [263–481]	1.2 [1.0–1.6]	0.11 [0.10–0.13]	1.1 [0.8–1.5]	0.30 [0.28–0.32]

was generally shallower compared to the mixed layer, computed from a density criterion, likely indicating decaying mixing due to daytime restratification (Brainerd and Gregg, 1995). The mixed layer was probably the result of previous mixing events, which could happen during nighttime convection. In several stations where density overturns (high L_T) reached deeper depths than strong ε (e.g. stations 7, 17, 23, 87, 116, 131), subsurface restratification in the temperature profiles (data not shown) and a L_T minimum were observed in the upper 20–25 m. These observations suggest that turbulence was suppressed in the upper 20–25 m by

daytime heating, whereas decaying turbulence remains below this depth, within the mixing layer.

These results show that during the seven months expedition we sampled different local meteorological conditions. Moreover, contrasting seasonal forcing was affecting the locations sampled at both hemispheres. For this reason, we cannot discard that the observed variability, both in the upper mixing layer and also in the ocean interior, in the described turbulence properties could be, at least partially, due to forcing mechanisms operating at different temporal scales. A complete analysis of the influence of temporal

variability in the described regional patterns, which is out of the scope of this study, would require longer datasets in order to understand the different scales of variability operating at each location.

4.2. Turbulence generating mechanisms in the ocean interior

In the ocean interior, shear instability, internal waves, and double-diffusion are potential mechanisms responsible for the generation of turbulence. Although the influence of different scales of temporal variability cannot be discarded (see above), clear regional patterns were observed in this layer associated with sampled hydrographic features.

One of the regions where shear instability has been reported to be a significant contribution to mixing is the Equatorial Undercurrent (EUC), a relatively strong ($> 0.1 \, \text{m s}^{-1}$) eastward subsurface current flowing in the equatorial Atlantic and Pacific oceans. LADCP data revealed that we sampled the influence of the EUC in the Atlantic (station 16) and the Pacific oceans (stations 93 and 94) (data not shown). The core of the EUC was located between 60 and 170 m in the Atlantic. In the Pacific, the upper limit of the current was located at approximately 100 m, and it extended below 300 m depth. Above the current core, both in the Atlantic and the Pacific, the surface flow was directed westward leading to a region of enhanced shear (Fig. 4). This region was observed at 50–80 m in the Atlantic and 90–140 m in the Pacific, with maximum values of $0.021–0.035 \, \text{s}^{-1}$ and $0.025 \, \text{s}^{-1}$, respectively. In the Atlantic, the lower boundary of the EUC at 170 m was also associated with enhanced shear ($\sim 0.015 \, \text{s}^{-1}$).

The effect of the EUC was sampled by the MSS profiler at the stations 16 in the Atlantic and 94 in the Pacific. At station 16 the effect of the EUC was noticed as enhanced ε (ca. $1 \times 10^{-6} \, \text{W kg}^{-1}$) was measured at about 40–65 m, coinciding with the upper boundary of the EUC (Fig. 5). Averaged ε computed in the ocean interior for this station ($9.9 \times 10^{-8} \, \text{W kg}^{-1}$) was one of the higher estimates reported during the expedition (Fig. 7). Lower values of ε (ca. $0.5 \times 10^{-8} \, \text{W kg}^{-1}$) were observed in the current core (80–105 m), in close agreement with the rates reported by Crawford (1976) for the same region. The signal of the EUC at station 94 was less intense, probably because this station was located further from the equator (Moum et al., 1986). Values of ε higher than $1 \times 10^{-7} \, \text{W kg}^{-1}$ were found between 80 and 100 m, near the upper boundary of the current. This is in good agreement with the value of $2 \times 10^{-7} \, \text{W kg}^{-1}$ reported by Moum et al. (1986), and one order of magnitude lower than the rates reported by Williams and Gibson (1974) ($8 \times 10^{-6} \, \text{W kg}^{-1}$).

The influence of the EUC was also visible in microstructure diffusivity data. Diffusivity estimates for stations 16 ($10 \times 10^{-4} \, \text{m}^2 \, \text{s}^{-1}$) and 94 ($7.5 \times 10^{-4} \, \text{m}^2 \, \text{s}^{-1}$) were among the higher estimates of the expedition. Averaged estimates for WTRA and PEQD were 2.27 and $3.62 \times 10^{-4} \, \text{m}^2 \, \text{s}^{-1}$, respectively, about one order of magnitude higher than the other provinces (see Table 1). Table 2 shows the contribution of the shear instability plus the internal waves term to total KPP diffusivity for each biogeographical province. The highest contribution also corresponded to the provinces including the equatorial regions in the Pacific (PEQD, $3.36 \times 10^{-4} \, \text{m}^2 \, \text{s}^{-1}$) and the Atlantic (WTRA, $1.48 \times 10^{-4} \, \text{m}^2 \, \text{s}^{-1}$) oceans.

In order to study the dependence of K_ρ in the ocean interior as a function of the Richardson number (Ri), which controls the onset of the shear Kelvin–Helmholtz instability (Miles, 1986), we used the parameterization proposed by Lozovatsky et al. (2006):

$$K_\rho = K_0 + \frac{K_M}{(1 + Ri/Ri_c)^n} \quad (15)$$

where $Ri = N^2 / ((\partial_z U)^2 + (\partial_z V)^2)$, with U and V being the horizontal
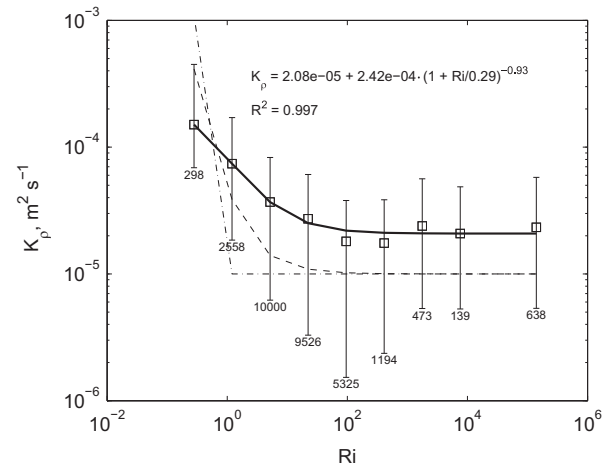

Fig. 11. Bin averaged diapycnal diffusivity (K_ρ) as a function of the Richardson number (Ri). The bars represent the 95% confidence intervals of diffusivity averages. The number of diffusivity samples used for computing the averages is indicated. The dark thick line represents the fit to the scaling equation proposed by Lozovatsky et al. (2006). The discontinuous line represents the Pacanowski and Philander (1981) model, and the dotted discontinuous line represents the KPP shear instability term (Large et al., 1994).

velocities computed from LADCP data, and Ri_c the critical Richardson number. K_0 is the background diffusivity when $Ri \to \infty$, and $K_0 + K_M$ the maximum diffusivity when $Ri \to 0$. K_ρ was bin averaged for different Ri and then fitted to the scaling model (Fig. 11). A good fit ($R^2 = 0.997$) was obtained for $K_0 = 0.21 \pm 0.02 \times 10^{-4} \, \text{m}^2 \, \text{s}^{-1}$, $K_M = 2.4 \pm 0.6 \times 10^{-4} \, \text{m}^2 \, \text{s}^{-1}$, $Ri_c = 0.29 \pm 0.24$ and $n = 0.93 \pm 0.23$. K_0 was comparable to, although slightly higher, background diffusivity by internal waves prescribed by the KPP proposed by Large et al. (1994) and Pacanowski and Philander (1981) ($0.1 \times 10^{-4} \, \text{m}^2 \, \text{s}^{-1}$), usually considered as the representative value of mixing in the pycnocline (Munk, 1966). Ri_c and the exponent n were also in good agreement with previously reported values, which ranged 0.1–0.25 and 1–3, respectively (Peters et al., 1988; Pacanowski and Philander, 1981; Lozovatsky et al., 2006). However, the roll-off towards the background internal wave diffusivity for high Ri was less steep than that predicted by the KPP.

The presence of salt fingers favorable stratification was studied by computing the density ratio $R_\rho = \alpha \partial_z T / \beta \partial_z S$. Stratification is favorable for salt fingers formation when warm and salty water overlies colder and fresher water, i.e. $1 < R_\rho < 100$. However, in oceanic environments, due to the perturbation by internal waves strain, salt fingers growth is only important for $1 < R_\rho < 2$ (St. Laurent and Schmitt, 1999). The bins where stratification conditions were favorable for salt fingers formation were in general more frequent in the Atlantic (8–57%) compared to the Pacific (0.1–7.1%) provinces (see Table 3). Bins where salt fingers were actively enhancing diffusivity were distinguished as those satisfying both $1 < R_\rho < 2$ and $\Gamma_{Obs} > 0.2$. In general, they only represented 10–20% of the bins with favorable stratification. As a result, heat diffusivity increased by 0.4–7.3% in the Atlantic provinces, as compared to the Osborn (1980) model (see Table 1). In the Pacific provinces, the increase was only significant at PNEC (ca. 5%). Salt finger active bins could not be determined at SPSG and PEQD, as no thermal variance dissipation rates were available for this leg (see Methods). However, very low contribution is expected for these provinces as the number of bins with favorable stratification was very low.

The use of the St. Laurent and Schmitt (1999) model to quantify the effect of salt fingers has a stronger influence in the diffusivity of dissolved substances (Table 3). For salt, the increase in diffusivity with respect to the Osborn (1980) model was 8–22% in the

Table 3

Percentage of bins where stratification was favorable for salt fingers formation (P_0^{sf}); active salt fingers (P^{sf}); heat ($\langle K_T^{tf} \rangle_{oi}$) and salt ($\langle K_S^{tf} \rangle_{oi}$) diffusivities in the ocean interior for salt fingers plus turbulence following the St. Laurent and Schmitt (1999) model. Diffusivities in the mixing layer ($\langle K_{SKIF-B} \rangle_{ml}$) and in the ocean interior ($\langle K_{SKIF-B} \rangle_{oi}$), according to the Bouffard and Boegman (2013) SKIF-B model are also included.

Prov.	P_0^{sf}	P^{sf}	$\langle K_T^{tf} \rangle_{oi}$ 10^{-4} (m² s⁻¹)	$\langle K_S^{tf} \rangle_{oi}$ 10^{-4} (m² s⁻¹)	$\langle K_{SKIF-B} \rangle_{ml}$ 10^{-4} (m² s⁻¹)	$\langle K_{SKIF-B} \rangle_{oi}$ 10^{-4} (m² s⁻¹)
NASE	56.9	5.8	0.471 [0.360–0.743]	0.498 [0.343–0.716]	4.27 [3.09–6.51]	0.176 [0.167–0.187]
NATR	20.7	4.6	0.168 [0.150–0.194]	0.187 [0.148–0.187]	1.46 [1.30–1.67]	0.099 [0.094–0.107]
WTRA	28.6	3.7	2.31 [1.40–3.75]	2.50 [1.48–3.89]	2.62 [2.07–3.88]	0.230 [0.203–0.262]
STAL	31.8	6.6	0.465 [0.431–0.526]	0.528 [0.431–0.546]	0.627 [0.475–1.003]	0.209 [0.189–0.298]
CARB	7.8	0.7	0.050 [0.043–0.064]	0.051 [0.044–0.066]	2.13 [1.80–2.82]	0.215 [0.044–0.717]
SPSG	0.4	–	–	–	3.19 [2.94–3.48]	0.118 [0.113–0.125]
PEQD	2.3	–	–	–	4.80 [3.29–10.20]	1.22 [0.89–1.60]
PNEC	0.1	0.1	0.132 [0.123–0.145]	0.142 [0.122–0.144]	1.90 [1.75–2.03]	0.099 [0.096–0.102]
NPTG	7.1	1.5	0.173 [0.146–0.237]	0.179 [0.147–0.236]	1.68 [1.56–1.86]	0.082 [0.078–0.086]

Atlantic provinces, except in CARB ($<2\%$). In the Pacific, the increase in PNEC and NPTG was 13% and 5%, respectively. These results are consistent with previous studies that have reported the relevance of salt fingers activity in the central waters of the Atlantic ocean (Schmitt, 1981; St. Laurent and Schmitt, 1999; Schmitt et al., 2005; Glessmer et al., 2008).

4.3. Comparison of microstructure and parameterization diffusivity estimates

In our study vertical diffusivity was estimated from observations of microstructure turbulence and also by using the K-profile parameterization (KPP). In general, both methods showed a good agreement both in the upper layer and in the ocean interior. The parameterization reproduced the vertical distribution of diffusivity, and the depth reached by intense mixing below the surface (boundary layer). In the ocean interior, the KPP captured the mixing enhancement due to sheared currents in the equatorial regions. However, due to the steep decrease in the shear instability term of diffusivity for $Ri > Ri_c$ (see Fig. 11) and the constant internal wave mixing term, part of the temporal and spatial variability of diffusivity was probably missed by the parameterization. In fact, compared with the KPP, microstructure diffusivity showed a smoother decrease for high Ri (Fig. 11). We included the scaling obtained by fitting our estimates of diapycnal diffusivity as a function of the Richardson number (see above) in the KPP, in order to verify the performance of this term to reproduce shear instability. This scaling produced lower diffusivity ($0.43 - 0.51 \times 10^{-4}$ m² s⁻¹) in the equatorial regions (WTRA, PEQD), compared to the original KPP and microstructure diffusivities, and it overestimated diffusivity in regions, as PNEC and NPTG, where the KPP showed a good agreement with microstructure diffusivity. Both parameterizations overestimated diffusivity in CARB. For these reasons, we conclude that the scaling was not able to significantly improve the KPP results.

On the other hand, KPP salt finger heat diffusivity was 0.73 and 0.24×10^{-4} m² s⁻¹ in NASE and SATL (Table 2), respectively, characterized by frequent favorable stratification for salt finger formation (Table 3). These values are about one order of magnitude higher than the difference between the St. Laurent and Schmitt (1999) and Osborn (1980) models (see Table 1 and Table 3). This observation supports that favorable stratification conditions do not necessarily involve that salt fingers are actively contributing to mixing. Hence, the KPP, where salt finger parameterization only depends on the density ratio (R_ρ), is likely to overestimate diffusivity in regions where stratification is favorable for salt finger formation.

The Osborn (1980) model, used in this study to compute diapycnal diffusivity from microstructure turbulence observations, assumes that mixing efficiency, $\Gamma = 0.2$, does not vary in time or space. In recent
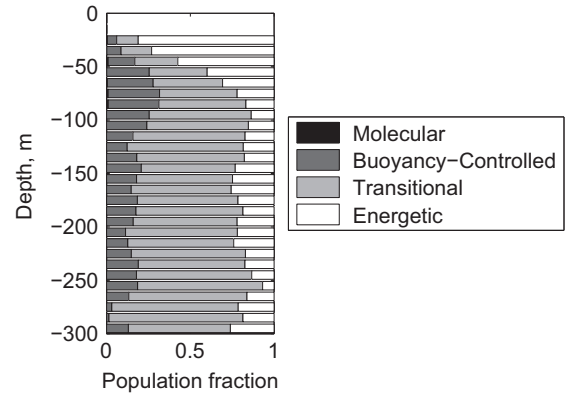

Fig. 12. Contribution of the different turbulence regimes as a function of the turbulence intensity parameter ($Re_b = \varepsilon/\nu N^2$) according to Bouffard and Boegman (2013): molecular ($Re_b < 1.7$), buoyancy-controlled ($1.7 < Re_b < 8.5$), transitional ($8.5 < Re_b < 100$) and energetic ($Re_b > 100$) regimes.

years increasing evidences accumulated from direct numerical simulations (DNS) and laboratory work (Barry et al., 2001; Smyth et al., 2001; Shih et al., 2005; Ivey et al., 2008) question this assumption. As a consequence, alternative parameterizations of diapycnal diffusivity based on ε but also depending on other turbulent properties have emerged (Ivey and Imberger, 1991; Shih et al., 2005; Bouffard and Boegman, 2013). The parameterization proposed by Shih et al. (2005) relies on the same assumptions than Osborn (1980) to solve the turbulent kinetic energy conservation equation (steady state and homogeneity), but allows Γ to vary with the turbulent intensity parameter $Re_b = \varepsilon/\nu N^2$ (where ν is the molecular viscosity, and N^2 the squared buoyancy frequency). This model, recently completed by Bouffard and Boegman (2013) (SKIF-B), parameterizes Γ (and hence K_ρ) as a function of Re_b in three different regimes: molecular ($Re_b < 7$), transitional ($7 < Re_b < 100$) and energetic ($Re_b > 100$). According to these authors, the Osborn (1980) formulation is only valid for the transitional regime, and the assumption of $\Gamma = 0.2$ in the other regimes would result in overestimated diffusivities.

The contribution of the different turbulence regimes, according to the classification proposed by Bouffard and Boegman (2013), as a function of the turbulent intensity parameter is shown in Fig. 12. The energetic regime dominates in the upper 50 m (ca. 60–80% of the bins), coinciding approximately with the base of the mixing layer. The transitional turbulence regime was dominant (ca. 60% of the bins) in the ocean interior, where the contribution of the energetic regime was ca. 20%. The maximum contribution of the buoyancy-controlled regime (ca. 20–30% of the bins) was in the 50–100 m depth range, corresponding to the seasonal thermocline. Large discrepancies are expected between the SKIF-B and Osborn (1980) models in the mixing layer due to the dominance of

the energetic regime. Averaged SKIF-B diffusivity for the mixing layer for the whole dataset was $1.50[1.38-1.77] \times 10^{-4} \, m^2 \, s^{-1}$ (see Table 3), two orders of magnitude lower compared to the estimates obtained from the Osborn, 1980 model (Table 1), and also from the KPP (Table 2). In the ocean interior, the agreement between both models was better, with averaged SKIF-B diffusivity $(0.22[0.19-0.25] \times 10^{-4} \, m^2 \, s^{-1})$ about half the averaged diffusivity computed from the Osborn (1980) model and the KPP. Diffusivity computed from the SKIF-B model in the mixing layer would require a mixing efficiency of about 0.001, much lower than suggested by old and recent observations (Oakey, 1982; Oakey and Greenan, 2004).

Although some studies have argued that the SKIF-B parameterization represents an improvement over the traditional Osborn (1980) formulation (Dunckley et al., 2012; Bouffard and Boegman, 2013), there is currently an open debate about its reliability due to, for example, the lack of agreement with tracer release inferred diffusivities (Gregg et al., 2012). It has been suggested that these discrepancies could be due to the fact that, for high Re_b, the laboratory and numerical domains were too small to include the Ozmidov scale (Kunze, 2011). In this regard, Bouffard and Boegman (2013) argued that the simulations by Shih et al. (2005) captured the Ozmidoz scale for $Re_b < 1000$. Furthermore, a decrease in mixing efficiency for high Re_b has been observed in atmospheric flux measurements (Lozovatsky and Fernando, 2013). A reconciliation between numerical simulations, laboratory work and field observations is required specially in the mixing layer, which controls the air–sea gas and heat exchanges.

5. Conclusions

Tracer release experiments (Ledwell et al., 1998) and microstructure measurements (Gregg, 1998) indicate that the magnitude of vertical diffusivity in the thermocline is only about $10^{-5} \, m^2 \, s^{-1}$. This value, comparable to the background internal waves diffusivity, is one order of magnitude lower than the values derived from the balance between the upwelling of cold water and the mixing down of warm water computed by ocean models (Munk, 1966). It has been proposed that this discrepancy could result from the episodic generation of mixing associated with tropical cyclones (Sriver and Huber, 2007), the interaction of ocean currents with the bottom topography (Rudnick et al., 2003), and also the swimming activity of marine organisms (Kunze et al., 2006a; Katija and Dabiri, 2009). Averaged diffusivity derived from microstructure observations collected during the Malaspina expedition in the ocean interior was about $0.2 \times 10^{-4} \, m^2 \, s^{-1}$ in the absence of shear instabilities, close to the reference value of $10^{-5} \, m^2 \, s^{-1}$. Higher diffusivities (ca. $10^{-4} \, m^2 \, s^{-1}$) were computed for the regions under the influence of strong shear associated with the Equatorial Undercurrent.

On average, the K-profile parameterization showed a good agreement with diffusivity estimates derived from microstructure observations using the Osborn (1980) model, both in the upper layer and in the ocean interior. Diffusivity derived from the SKIF-B model, recently proposed by Bouffard and Boegman (2013), was comparable to the values computed from the Osborn model in the ocean interior, whereas in the mixing layer estimates from the SKIF-B model were two orders of magnitude lower. This discrepancy could have important implications for the transport of heat and gases through the air–sea interface.

Favorable conditions for salt finger formation were more frequent in the Atlantic basin. According to the St. Laurent and Schmitt (1999) model the consideration of double diffusion slightly increased temperature diffusivity with respect to the Osborn (1980) model. However, for dissolved substances as salt and nutrients, diffusivity increased about 10–20% in the Atlantic provinces. Because salt fingers mix heat

and dissolved substances more efficiently than mechanical turbulence, the consideration of this process could have important implications for the transport of properties and substances, and derived biogeochemical impacts. Hamilton et al. (1989) argued that nitrate fluxes into the photic zone in subtropical regions could be underestimated up to one order of magnitude if salt fingers mixing was ignored. By using a modeling approach, Glessmer et al. (2008) showed that the nutrient input through double-diffusion has a significant influence in primary and export production in oligotrophic regions, generating an additional oceanic carbon uptake of about $0.4 \, g \, C \, m^2 \, year^{-1}$. According to these authors, salt fingers and mechanical mixing have different climate sensitivities, and its relative contribution to mixing will probably be subjected to changes in the future.

Small-scale turbulence strongly affects the overall ocean circulation, influences the marine biota through the control on the distribution and growth of marine organisms, and helps to disperse pollutants (Thorpe, 2004). Climate models predict changes in the intensity of mixing and stratification as a consequence of global warming (Sarmiento et al., 1998). For this reason, understanding the regional and temporal variability of turbulent mixing is crucial to predict changes in ocean circulation and global biogeochemical cycles in the near future. In this sense, the microstructure turbulence data collected during the Malaspina expedition represents a unique contribution to progress in our knowledge about the distribution of turbulence in the ocean, and its interaction with other chemical and biological processes.

Appendix A. Supplementary data

Supplementary data associated with this paper can be found in the online version at http://dx.doi.org/10.1016/j.dsr.2014.08.006.

References

Arcos-Pulido, M., Rodríguez-Santana, A., Emelianov, M., Paka, V., Arístegui, J., Benavides, M., Sangrá, P., Machín, F., García-Weil, L., Estrada-Allis, S., 2014. Diapycnal nutrient fluxes on the northern boundary of Cape Ghir upwelling region. Deep Sea Res. Part I 840, 100–109.

Baker, M.A., Gibson, C.H., 1987. Sampling turbulence in the stratified ocean: statistical consequences of strong intermittency. J. Phys. Oceanogr. 17 (10), 1817–1836 http://dx.doi.org/10.1175/1520-0485(1987)017⟨1817:STITSO⟩2.0.CO;2.

Barry, M.E., Ivey, G.N., Kraig, B.W., Imberger, J., 2001. Measurements of diapycnal diffusivities in stratified fluids. J. Fluid Mech. 442, 267–291. http://dx.doi.org/10.1017/S0022112001005080.

Belcher, S.E., Grant, A.L.M., Hanley, K.E., Fox-Kemper, B., Van Roekel, L., Sullivan, P.P., Large, W.G., Brown, A., Hines, A., Calvert, D., Rutgersson, A., Pettersson, H., Bidlot, J.-R., Janssen, P.A.E.M., Polton, J.A., 2012. A global perspective on Langmuir turbulence in the ocean surface boundary layer. Geophys. Res. Lett. 39 (18), L18605.

Bouffard, D., Boegman, L., 2013. A diapycnal diffusivity model for stratified environmental flows. Dynam. Atmos. Oceans 61–62, 14–34. http://dx.doi.org/10.1016/j.dynatmoce.2013.02.002.

Brainerd, K.E., Gregg, M.C., 1995. Surface mixed and mixing layer depths. Deep Sea Res. Part I 42 (9), 1521–1543.

Chisholm, S.W., 1992. Phytoplankton Size in Primary Productivity and Biogeochemical Cycles in the Sea. Plenum, New York, pp. 213–237.

Crawford, W.R., 1976. Turbulent Energy Dissipation in the Atlantic Equatorial Undercurrent (Ph.D. thesis). Institute of Oceanography, The University of British Columbia.

Cuypers, Y., Bouruet-Aubertot, P., Marec, C., Fuda, J.-L., 2012. Characterization of turbulence from a fine-scale parameterization and microstructure measurements in the mediterranean sea during the BOUM experiment. Biogeosciences 9 (8), 3131–3149. http://dx.doi.org/10.5194/bg-9-3131-2012.

Davis, R.E., 1996. Sampling turbulent dissipation. J. Phys. Oceanogr. 26, 341–358.

Dietze, H., Oschlies, A., Kähler, P., 2004. Internal-wave induced and double-diffusive nutrient fluxes to the nutrient-consuming surface layer in the oligotrophic subtropical north atlantic. Ocean Dyn. 54, 1–7. http://dx.doi.org/10.1007/s10236-003-0060-9.

Doubell, M.J., Prairie, J.C., Yamazaki, H., 2012. Millimeter scale profiles of chlorophyll fluorescence: deciphering the microscale spatial structure of phytoplankton. Deep Sea Res. Part II. 101:207–215. http://dx.doi.org/10.1016/j.dsr2.2012.12.009.

Dunckley, J.F., Koseff, J.R., Steinbuck, J.V., Monismith, S.G., Genin, A., 2012. Comparison of mixing efficiency and vertical diffusivity models from temperature microstructure. J. Geophys. Res. Oceans 117 (C10), C10008. http://dx.doi.org/10.1029/2012JC007967.

Falkowski, P.G., Oliver, M.J., 2007. Mix and match: how climate selects phytoplankton. Nat. Rev. Microbiol. 5 (10), 813–819. http://dx.doi.org/10.1038/nrmicro1751.

Fischer, J., Visbeck, M., 1993. Deep velocity profiling with self-contained ADCPs. J. Atmos. Ocean Technol. 10 (5), 764–773. http://dx.doi.org/10.1175/1520-0426(1993)010⟨0764:DVPWSC⟩2.0.CO;2.

Fischer, T., 2011. Diapycnal Diffusivity and Transport of Matter in the Open Ocean Estimated from Underway Acoustic Profiling and Microstructure Profiling (Ph.D. thesis). Leibniz Institute of Marine Sciences (GEOMAR), University of Kiel, Germany.

Fischer, T., Banyte, D., Brandt, P., Dengler, M., Krahmann, G., Tanhua, T., Visbeck, M., 2013. Diapycnal oxygen supply to the tropical north atlantic oxygen minimum zone. Biogeosciences 10 (7), 5079–5093.

Gargett, A.E., 1989. Ocean turbulence. Ann. Rev. Fluid Mech. 21, 419–451. http://dx.doi.org/10.1146/annurev.fl.21.010189.002223.

Glessmer, M.S., Oschlies, A., Yool, A., 2008. Simulated impact of double-diffusive mixing on physical and biogeochemical upper ocean properties. J. Geophys. Res. Oceans 113 (C8), C08029. http://dx.doi.org/10.1029/2007JC004455.

Gregg, M., Alford, M., Kontoyiannis, H., Zervakis, V., Winkel, D., 2012. Mixing over the steep side of the Cycladic Plateau in the Aegean Sea. J. Mar. Syst. 89 (1), 30–47. http://dx.doi.org/10.1016/j.jmarsys.2011.07.009.

Gregg, M.C., 1989. Scaling turbulent dissipation in the thermocline. J. Geophys. Res. 94 (C7), 9686–9698. http://dx.doi.org/10.1029/JC094iC07p09686.

Gregg, M.C., 1998. Estimation and Geography of Diapycnal Mixing in the Stratified Ocean Coastal Estuarine Studies, vol. 54. AGU, Washington, DC, pp. 305–338. http://dx.doi.org/10.1029/CE054p0305.

Gregg, M.C., Sanford, T.B., Winkel, D.P., 2003. Reduced mixing from the breaking of internal waves in equatorial waters. Nature 422 (6931), 513–515. http://dx.doi.org/10.1038/nature01507.

Haidvogel, D., Arango, H., Budgell, W., Cornuelle, B., Curchitser, E., Di Lorenzo, E., Fennel, K., Geyer, W., Hermann, A., Lanerolle, L., Levin, J., McWilliams, J., Miller, A., Moore, A., Powell, T., Shchepetkin, A., Sherwood, C., Signell, R., Warner, J., Wilkin, J., 2008. Ocean forecasting in terrain-following coordinates: formulation and skill assessment of the regional ocean modeling system. J. Comput. Phys. 227 (7), 3595–3624. http://dx.doi.org/10.1016/j.jcp.2007.06.016.

Hamilton, J.M., Lewis, M.R., Ruddick, B.R., 1989. Vertical fluxes of nitrate associated with salt fingers in the world's oceans. J. Geophys. Res. Oceans 94 (C2), 2137–2145. http://dx.doi.org/10.1029/JC094iC02p02137.

Henyey, F.S., Wright, J., Flatté, S.M., 1986. Energy and action flow through the internal wave field: an Eikonal approach. J. Geophys. Res. 91 (C7), 8487–8495. http://dx.doi.org/10.1029/JC091iC07p08487.

Hibiya, T., Nagasawa, M., Niwa, Y., 2007. Latitudinal dependence of diapycnal diffusivity in the thermocline observed using a microstructure profiler. Geophys. Res. Lett. 34 (24), L24602. http://dx.doi.org/10.1029/2007GL032323.

Ivey, G.N., Imberger, J., 1991. On the nature of turbulence in a stratified fluid Part I: the energetics of mixing. J. Phys. Oceanogr. 21 (5), 650–658. http://dx.doi.org/10.1175/1520-0485(1991)021⟨0650:OTNOTI⟩2.0.CO;2.

Ivey, G.N., Winters, K.B., Koseff, J.R., 2008. Density stratification, turbulence, but how much mixing? Annu. Rev. Fluid Mech. 40 (1), 169–184. http://dx.doi.org/10.1146/annurev.fluid.39.050905.110314.

Jackson, L., Hallberg, R., Legg, S., 2008. A parameterization of shear-driven turbulence for ocean climate models. J. Phys. Oceanogr. 38 (5), 1033–1053. http://dx.doi.org/10.1175/2007JPO3779.1.

Jurado, E., Dijkstra, H.A., van der Woerd, H.J., 2012a. Microstructure observations during the spring 2011 Stratiphyt-II cruise in the northeast Atlantic. Ocean Sci. 9 (3), 2153–2186. http://dx.doi.org/10.1029/2011JC007137.

Jurado, E., vanderWoerd, H.J., Dijkstra, H.A., 2012b. Microstructure measurements along a quasi-meridional transect in the northeastern Atlantic ocean. J. Geophys. Res. 117 (C4), C04016. http://dx.doi.org/10.5194/osd-9-2153-2012.

Katija, K., Dabiri, J.O., 2009. A viscosity-enhanced mechanism for biogenic ocean mixing. Nature 460 (7255), 624–626. http://dx.doi.org/10.1038/nature08207.

Kelley, D.E., 1990. Fluxes through diffusive staircases: a new formulation. J. Geophys. Res. 95 (C3), 3365–3371. http://dx.doi.org/10.1029/JC095iC03p03365.

Kunze, E., 2011. Fluid mixing by swimming organisms in the low-Reynolds-number limit. J. Mar. Res. 69 (4–5), 591–601.

Kunze, E., Dower, J.F., Beveridge, I., Dewey, R., Bartlett, K.P., 2006a. Observations of biologically generated turbulence in a coastal inlet. Science 313 (5794), 1768–1770. http://dx.doi.org/10.1126/science.1129378.

Kunze, E., Firing, E., Hummon, J.M., Chereskin, T.K., Thurnherr, A.M., 2006b. Global abyssal mixing inferred from lowered ADCP shear and CTD strain profiles. J. Phys. Oceanogr. 36 (8), 1553–1576. http://dx.doi.org/10.1175/JPO2926.1.

Large, W.G., McWilliams, J.C., Doney, S.C., 1994. Oceanic vertical mixing: A review and a model with a nonlocal boundary layer parameterization. Rev. Geophys. 32 (4), 363–403. http://dx.doi.org/10.1029/94RG01872.

Ledwell, J.R., Watson, A.J., Law, C.S., 1998. Mixing of a tracer in the pycnocline. J. Geophys. Res. Oceans 103 (C10), 21499–21529. http://dx.doi.org/10.1029/98JC01738.

Lewis, M., Hebert, D., Harrison, W., Platt, T., Oakey, N., 1986. Vertical nitrate fluxes in the oligotrophic ocean. Science 234 (4778), 870–873. http://dx.doi.org/10.1126/science.234.4778.870.

Longhurst, A.R., 2006. Ecological Geography of the Sea, 2n ed. Academic Press, San Diego.

Lozovatsky, I., Fernando, H., 2013. Mixing efficiency in natural flows. Phil. Trans. R. Soc. A 371 (1982), 21499–21529.

Lozovatsky, I., Roget, E., Fernando, H., Figueroa, M., Shapovalov, S., 2006. Sheared turbulence in a weakly stratified upper ocean. Deep Sea Res. Part I 53 (2), 387–407.

Maar, M., Nielsen, T.G., Stips, A., Visser, A.W., 2003. Microscale distribution of zooplankton in relation to turbulent diffusion. Limnol. Oceanogr. 48, 1312–1325. http://dx.doi.org/10.4319/lo.2003.48.3.1312.

McDougall, T.J., 1988. Some Implications of Ocean Mixing for Ocean Modelling in Elsevier Oceanography Series, vol. 46. Elsevier, New York, pp. 21–35. http://dx.doi.org/10.1016/S0422-9894(08)70535-X.

Miles, J., 1986. Richardson's criterion for the stability of stratified shear flow. Phys. Fluids 29 (10), 3470–3471.

Mellor, G.L., Yamada, T., 1982. Development of a turbulence closure model for geophysical fluid problems. Rev. Geophys. 20 (4), 851–875.

Moum, J.N., Osborn, T.R., Crawford, W.R., 1986. Pacific equatorial turbulence: revisited. J. Phys. Oceanogr. 16, 1516–1523. http://dx.doi.org/10.1175/1520-0485(1986)016⟨1516:PETR⟩2.0.CO;2.

Moum, J.N., Smyth, W.D., 2001. Upper Ocean Mixing. Academic Press, Oxford, p. 3093.

Mouriño–Carballido, B., Marañón, E., Fernández, A., Graña, R., Bode, A., Varela, V., Domínguez, F., Escánez, J., deArmas, D., 2011. Importance of N_2 fixation versus nitrate eddy diffusion across the Atlantic Ocean. Limnol. Oceanogr. 56 (3), 999–1007. http://dx.doi.org/10.4319/lo.2011.56.3.0999.

Munk, W., Wunsch, C., 1998. Abyssal recipes II: energetics of tidal and wind mixing. Deep Sea Res. Part I 45 (12), 1977–2010. http://dx.doi.org/10.1016/S0967-0637(98)00070-3.

Munk, W.H., 1966. Abyssal recipes. Deep Sea Res. Oceanogr. Abstr. 13 (4), 707–730. http://dx.doi.org/10.1016/0011-7471(66)90602-4.

Oakey, N.S., 1982. Determination of the rate of dissipation of turbulent energy from simultaneous temperature and velocity shear microstructure measurements. J. Phys. Oceanogr. 12 (3), 256–271.

Oakey, N.S., Greenan, B.J.W., 2004. Mixing in a coastal environment: 2. a view from microstructure measurements. J. Geophys. Res. Oceans 109 (C10), C10014.

Osborn, T.R., 1980. Estimates of the local rate of vertical diffusion from dissipation measurements. J. Phys. Oceanogr. 10, 83–89. http://dx.doi.org/10.1175/1520-0485(1980)010⟨0083:EOTLRO⟩2.0.CO;2.

Osborn, T.R., Cox, C.S., 1972. Oceanic fine structure. Geophys. Fluid Dyn. 3 (1), 321–345.

Pacanowski, R.C., Philander, S.G.H., 1981. Parameterization of vertical mixing in numerical models of tropical oceans. J. Phys. Oceanogr. 11, 1443–1451. http://dx.doi.org/10.1175/1520-0485(1981)011⟨1443:POVMIN⟩2.0.CO;2.

Paulson, C.A., Simpson, J.J., 1977. Irradiance measurements in the upper ocean. J. Phys. Oceanogr. 7 (6), 952–956. http://dx.doi.org/10.1175/1520-0485(1977)007⟨0952:IMITUO⟩2.0.CO;2.

Peters, H., Gregg, M.C., Toole, J.M., 1988. On the parameterization of equatorial turbulence. J. Geophys. Res. Oceans 93 (C2), 1199–1218.

Prandke, H., Holtsch, K., Stips, A., 2000. MITEC Technology Development: The Microstructure/Turbulence Measuring System MSS. Space Applications Institute, Ispra.

Prandke, H., Stips, A., 1998. Test measurements with an operational microstructure-turbulence profiler: detection limit of dissipation rates. Aquat. Sci. 60, 191–209. http://dx.doi.org/10.1007/s000270050036.

Rainville, L., Winsor, P., 2008. Mixing across the Arctic Ocean: Microstructure observations during the Beringia 2005 expedition. Geophys. Res. Lett. 35 (8), L08606. http://dx.doi.org/10.1029/2008GL033532.

Rudnick, D.L., Boyd, T.J., Brainard, R.E., Carter, G.S., Egbert, G.D., Gregg, M.C., Holloway, P.E., Klymak, J.M., Kunze, E., Lee, C.M., Levine, M.D., Luther, D.S., Martin, J.P., Merrifield, M.A., Moum, J.N., Nash, J.D., Pinkel, R., Rainville, L., Sanford, T.B., 2003. From tides to mixing along the Hawaiian Ridge. Science 301 (5631), 355–357. http://dx.doi.org/10.1126/science.1085837.

Sanchez, X., Roget, E., Planella, J., Forcat, F., 2011. Small-scale spectrum of a scalar field in water: the Batchelor and Kraichnan models. J. Phys. Oceanogr. 41 (11), 2155–2167.

Sarmiento, J.L., Hughes, T.M.C., Stouffer, R.J., Manabe, S., 1998. Simulated response of the ocean carbon cycle to anthropogenic climate warming. Nature 393 (6682), 245–249. http://dx.doi.org/10.1038/30455.

Schafstall, J., Dengler, M., Brandt, P., Bange, H., 2010. Tidal-induced mixing and diapycnal nutrient fluxes in the Mauritanian upwelling region. J. Geophys. Res. 115 (C10), C10014. http://dx.doi.org/10.1029/2009JC005940.

Schmitt, R.W., 1981. Form of the temperature-salinity relationship in the central water: evidence for double-diffusive mixing. J. Phys. Oceanogr. 11 (7), 1015–1026. http://dx.doi.org/10.1175/1520-0485(1981)011⟨1015:FOTTSR⟩2.0.CO;2.

Schmitt, R.W., Ledwell, J.R., Montgomery, E.T., Polzin, K.L., Toole, J.M., 2005. Enhanced diapycnal mixing by salt fingers in the thermocline of the Tropical Atlantic. Science 308 (5722), 685–688. http://dx.doi.org/10.1126/science.1108678.

Sharples, J., Moore, C.M., Hickman, A.E., Holligan, P.M., Tweddle, J.F., Palmer, M.R., Simpson, J.H., 2009. Internal tidal mixing as a control on continental margin ecosystems. Geophys. Res. Lett. 36 (23), L23603. http://dx.doi.org/10.1029/2009GL040683.

Shih, L.H., Koseff, J.R., Ivey, G.N., Ferziger, J.H., 2005. Parameterization of turbulent fluxes and scales using homogeneous sheared stably stratified turbulence simulations. J. Fluid Mech. 525, 193–214. http://dx.doi.org/10.1017/S0022112004002587.

Smyth, W.D., Moum, J.N., Caldwell, D.R., 2001. The efficiency of mixing in turbulent patches: Inferences from direct simulations and microstructure observations. J. Phys. Oceanogr. 31 (8), 1969–1992. http://dx.doi.org/10.1175/1520-0485(2001)031⟨1969:TEOMIT⟩2.0.CO;2.

Sriver, R.L., Huber, M., 2007. Observational evidence for an ocean heat pump induced by tropical cyclones. Nature 447 (7144), 577–580. http://dx.doi.org/10.1038/nature05785.

St. Laurent, L., Schmitt, R.W., 1999. The contribution of salt fingers to vertical mixing in the North Atlantic Tracer Release Experiment*. J. Phys. Oceanogr. 29 (7), 1404–1424. http://dx.doi.org/10.1175/1520-0485(1999)029⟨1404:TCOSFT⟩2.0.CO;2.

Thorpe, S.A., 1977. Turbulence and mixing in a Scottish loch. Phil. Trans. R. Soc. Lond. A 286 (1334), 125–181.

Thorpe, S.A., 2004. Recent developments in the study of ocean turbulence. Annu. Rev. Earth Planet. Sci. 20 (32), 91–109. http://dx.doi.org/10.1146/annurev.earth.32.071603.152635.

Williams, R.B., Gibson, C.H., 1974. Direct measurements of turbulence in the Pacific Equatorial Undercurrent. J. Phys. Oceanogr. 4, 104–108. http://dx.doi.org/10.1175/1520-0485(1974)004⟨0104:DMOTIT⟩2.0.CO;2.

Wunsch, C., Ferrari, R., 2004. Vertical mixing, energy, and the general circulation of the oceans. Annu. Rev. Fluid Mech. 36, 281–314. http://dx.doi.org/10.1146/annurev.fluid.36.050802.122121.